

Student thesis series INES nr 525

Assessing annual forest phenology: A comparison of Unmanned Aerial Vehicle (UAV) and phenocamera datasets

Shangharsha Thapa

2020
Department of
Physical Geography and Ecosystem Science
Lund University
Sölvegatan 12
S-223 62 Lund
Sweden



Shangharsha Thapa (2020).

Assessing annual forest phenology: A comparison of Unmanned Aerial Vehicle (UAV) and phenocamera datasets

Master degree thesis, 30 credits in Masters of *Geomatics*

Department of Physical Geography and Ecosystem Science, Lund University

Level: Master of Science (MSc)

Course duration: *January* 2020 until *June* 2020

Disclaimer

This document describes work undertaken as part of a program of study at the University of Lund. All views and opinions expressed herein remain the sole responsibility of the author, and do not necessarily represent those of the institute.

Assessing annual forest phenology: A comparison of Unmanned Aerial Vehicle (UAV) and phenocamera datasets

Shangharsha Thapa

Master thesis, 30 credits, in *Master's Program in Geomatics*

Supervisors:

Virginia Garcia-Millan

Lars Eklundh

Department of Physical Geography and Ecosystem Science,
Lund University

Exam committee:

Torbern Tagesson

Jutta Holst

Department of Physical Geography and Ecosystem Science,
Lund University

Table of Contents

List of Figures	iv
List of Tables	vi
List of Abbreviations	vii
1 Introduction.....	1
2 Aim	2
3 Background.....	3
3.1 Remote sensing of vegetation phenology	3
3.2 Near-surface remote sensing derived phenology	3
3.3 UAV remote sensing.....	5
4 Materials and Methods.....	7
4.1 Study Area	7
4.2 Datasets	8
4.2.1 Phenology Cameras	8
4.2.2 UAV	9
4.2.3 Spectral Sensor.....	11
4.3 Methods.....	13
4.3.1 Data Processing.....	14
4.3.1.1 Phenocamera Image Processing.....	14
4.3.1.2 UAV Image Processing.....	17
4.3.1.3 Spectral Sensor Data Processing.....	22
4.3.1.4 Phenology dates from time series data.....	24
4.3.2 Inter-comparison and validation	27
5 Result	29
5.1 Comparison of UAV and Spectral Sensor-derived NDVI.....	29
5.2 Comparison of Phenocamera-based VIs with spectral sensor NDVI	30
5.3 Comparison of Phenocamera-based VIs with UAV-NDVI.....	32
5.4 Annual variability of VIs from Phenocamera	33
5.4 Variability of VI trajectories within different ROI	34
5.5 Phenological dates estimated from different platforms	35
6 Discussion	37
7 Conclusions.....	42
8 Recommendations.....	44
References.....	46
Supplementary Data.....	51

List of Figures

- Figure 1. Schematic diagram of a generic phenocamera deployment plan at a forested research site. The camera is placed on a tower taller than the vegetation, with a field of view (FOV) across the landscape oriented towards north to minimize lens flare and shadows. A spectral reflectance sensor is also mounted on the tower, which measures NDVI. Images captured by the system are uploaded to the server once a day via internet (modified after Richardson et al., 2013b).*..... 5
- Figure 2. Map showing the location of Asa Research Station, Digital Surface Model (DSM) of the site, UAV Orthomosaic (lower right) and a sample phenocamera image (upper right).*..... 7
- Figure 3. Sample Phenocamera image captured on 05/24/2019 (Source: SITES)* 8
- Figure 4. Parrot Sequoia multispectral sensor (left) and Sunshine sensor (right), Source: Sequoia manual* 10
- Figure 5. Spectral Reflectance Sensor for NDVI. Cosine corrected hemispherical sensor (left) and Field-stop lens sensor (right). Source: <http://www.metergroup.com>* 12
- Figure 6. Overall workflow of the research. The workflow is the combined steps of four processing steps to achieve the objective of current research: data collection, data processing, inter-comparison and lastly the validation of those results.* 13
- Figure 7. Region of Interest for extracting time series of RGB DN Triplets (each colored rectangle refers to a different ROI). Red and yellow colored rectangles represent ROI that are close to the camera and represent individual spruce tree canopies. The blue one represents a ROI with understory vegetation including shadows, while the green rectangle represents the ROI that is far away from the camera, close to horizon. Finally, the white rectangle represents the dominant FOV of the images. (Image Source: SITES)* 15
- Figure 8. Example time series of phenocamera GCC for defined ROI. Grey circles are all image average GCC (every hour) value within ROI; blue circles are average GCC for snow covered images and red triangles are 1-day (a) and 3-day (b) average GCC values.* 16
- Figure 9. Sunshine sensor data plot showing variation of irradiance within UAV mission* 17
- Figure 10. Image processing workflow in Photoscan for generating Orthophotos* 19
- Figure 11. UAV orthomosaic of the study area. One orthomosaic (left) is from 16th April, 2018 and the other (right) is from 26th April, 2019. Yellow dashed polygon represents the main experimental forest area.*..... 19
- Figure 12. Variation of mean DN values at different stages of UAV mission in relation with sensor temperature. Note that mean DN values plotted here refers to only 5% reflectance panel on NIR band* 21
- Figure 13. NDVI maps for the year 2018 & 2019. Dashed ellipse (red) refers to the spectral sensor footprint.* 22
- Figure 14. Plot of NDVI measurements from spectral sensor for year 2018 (a) and 2019 (b). Grey dots represent all the NDVI values between 10 a.m.- 2 p.m. while hollow circle symbol (red) represents the average NDVI values every 3 day over the study period.*

Red circle within dashed ellipse represent NDVI values on snowy day which were avoided from the analysis.23

Figure 15. Double logistic fit of 3-day averaged time series of GCC (a), ExG (b), VIgreen (c) and retrieval of phenological transition date from the fit. Green (solid, dashed dot, dashed) lines represent SOS, MOS & EOS while red (solid, dashed dot, dashed) lines represent SOF, MOF and EOF events respectively.26

Figure 16. Spline interpolation fit of UAV-derived NDVI time series and retrieval of phenological transition date from the fit. Green (solid, dashed dot, dashed) lines represent SOS, MOS and EOS, while red (solid, dashed dot, dashed) lines represent SOF, MOF and EOF events, respectively. Upper plot and lower plot represent 2018 and 2019, respectively.27

Figure 17. NDVI values extracted from UAV (blue square markers) and spectral sensor (green dot markers) while the red symbols (triangle) represents smoothed UAV-NDVI values of 2018 (a) and 2019 (b) used for curve fitting process.30

Figure 18. Time series of spectral sensor NDVI (black dots for 2018, blue circles for 2019) and phenocamera-based VIs namely GCC (a), ExG (b) and VIgreen (c). The y-axis is a normalized scale from indices minimum to maximum values while x-axis is the temporal period of observations. Gap in time series of spectral sensor NDVI refers to removal of low measurements on a snowy day.31

Figure 19. Time series of phenocamera based VIs namely GCC (a), ExG (b) and VIgreen (c) versus UAV-NDVI for both year 2018 and 2019. The y-axis is a normalized scale from indices minimum to maximum values while x-axis is the temporal period of observations. Filled circles (black) and hollow circles (black) represent UAV-NDVI for 2018 and 2019 respectively.32

Figure 20. Vegetation indices profiles for 2018 between two different ROIs within phenocamera FOV. Y-axis represents the normalized scale to make VI values appear between 0 and 1.34

List of Tables

<i>Table 1. Detailed specifications of UAV system. The UAV system was a quadcopter with flight endurance upto 25 minutes at 1.2 kg take-off weight.</i>	9
<i>Table 2. Parrot Sequoia Camera Specifications (Source: Parrot Sequoia, User Manual: http://www.parrot.com).</i>	10
<i>Table 3. Information on the UAV missions conducted during 2018 and 2019 with corresponding number of images and weather conditions.</i>	51
<i>Table 4. Measurement specifications of SRS-NDVI sensor</i>	12
<i>Table 5. Pearson's correlation coefficient between UAV-NDVI and spectral sensor NDVI for the years 2018 and 2019</i>	29
<i>Table 6. Correlation between phenocamera vegetation indices over full field of view (FOV) versus spectral sensor derived NDVI values computed within overlapping foot print of sensor with the phenocamera and UAV-derived NDVI, using Pearson's correlation value</i>	31
<i>Table 7. Correlation among phenocamera-based indices: GCC, ExG, and VIgreen</i>	33
<i>Table 8. Phenocamera-derived VIs (GCC, ExG, VIgreen), spectral sensor-NDVI and UAV-NDVI estimates of Start Of Spring (SOS), Middle Of Spring (MOS), End Of Spring (EOS), Start Of Fall (SOF), Middle Of Fall (MOF), End Of Fall (EOF), visual inspection and maximum of season (MAX) day of year</i>	35

List of Abbreviations

DN	Digital Number
DSM	Digital Surface Model
EOF	End of Fall
EOS	End of Spring
EVI	Enhanced Vegetation Index
ExG	Excess Green Index
EXIF	Exchangeable Image File Format
FOV	Field of View
G	Green
GCC	Green Chromatic Coordinate
GCP	Ground Control Points
GCT	Ground Calibration Targets
GDAL	Geospatial Data Abstraction Library
GPP	Gross Primary Productivity
GPS	Global Positioning System
HFOV	Horizontal Field of View
MP	Megapixels
NIR	Near Infrared
NDVI	Normalized Difference Vegetation Index
R	Red
RE	Red Edge
ROI	Region of Interest
RMSE	Root Mean Square Error
SOF	Start of Fall
SOS	Start of Spring
SRS	Spectral Reflectance Sensor
SITES	Swedish Infrastructure for Ecosystem Science
UAV	Unmanned Aerial Vehicle
VI _s	Vegetation Indices
VI _{green}	Normalized Difference of green and red bands

Abstract

Near-surface remote sensing platforms such as Unmanned Aerial Vehicles (UAVs) and phenocameras appear to be potential platforms for keeping track of seasonal dynamics at a local scale. This research focusses on extracting time series of different vegetation indices (VIs) from both platforms, computing seasonality events from them and comparing the results against spectral sensor data.

Time series of UAV derived Normalized Difference Vegetation Index (NDVI) and phenocamera based Green Chromatic Coordinate (GCC), Excess Green Index (ExG) and Normalized Difference of Green & Red (VIgreen) indices were extracted for growing season of years 2018 and 2019. There was a good agreement between the UAV and spectral sensor-derived NDVI as reflected in high Pearson's correlation coefficients ($r_{2018} = 0.780$ and $r_{2019} = 0.903$). Phenocamera-based GCC best approximates NDVI measurements from the spectral sensor, with correlation coefficients of $r_{2018} = 0.848$ and $r_{2019} = 0.80$, closely followed by ExG ($r_{2018} = 0.777$ and $r_{2019} = 0.798$), while they were lowest in the case of VIgreen ($r_{2018} = 0.719$ and $r_{2019} = 0.773$). Due to small number of records, UAV-derived NDVI, led to slightly lower correlation coefficients when compared with phenocamera VIs, with GCC and ExG being the best ($r_{2018} = 0.670$, $r_{2018} = 0.695$), while no correlation exists for the year 2019 ($\rho > 0.05$). Time series data were fitted with double logistic function for spectral sensor NDVI and phenocamera-based VIs, whereas a spline interpolation method was employed to fit UAV-NDVI time series. Despite, the offset between spectral sensor NDVI and UAV-NDVI in 2018, the UAV curve follows nicely the spectral sensor curve except for the year 2019. GCC, ExG, and UAV-NDVI based phenological transition dates estimation were consistently more closely associated with the visual assessments of phenology, at an accuracy of less than 8 days with year 2019 as an exception where Start Of Spring (SOS) was 14 days earlier. SOS from VIgreen and spectral sensor NDVI occurred earlier (24 and 27 days respectively), compared to visually observed phenophase dates. The transition dates from all platforms over the study period revealed a shift ranging between 6 – 12 days in all seasonality events. Due to hourly temporal resolution of phenocamera, it provided more flexibility in estimating important phenophase dates. Tree-canopies level quality information including NDVI can be obtained with high temporal resolution and large spatial coverage of UAV, unmatched by any other methods discussed. The agreement between UAV-NDVI and spectral sensor NDVI for evergreen spruce forest

reveals the adequacy of these platforms for the monitoring of tree dynamics. In addition, phenocameras demonstrated to offer a detailed insight into plant phenology at fine spatio-temporal scales.

Keywords: Geography, Ecosystem Analysis, Near-surface Remote Sensing, UAV, Phenocamera, Forest Phenology, Phenophase, Seasonality, NDVI, GCC

Acknowledgement

I would like to express my gratitude to all those who gave me the opportunity to complete this thesis. I appreciate the Lund University Global Scholarship Committee for providing me a two-year scholarship for pursuing Master's degree in Geomatics at the Department of Physical Geography and Ecosystem Science, Lund University.

I offer my sincere thanks to my supervisor Dr. Virginia Garcia Millan and Dr. Lars Eklundh for the continuous support and encouragement, guidance and patience throughout the entire thesis period. I feel very grateful to learn and improve my understanding of remote sensing by working under you. The research skills learnt from both of you will benefit me in the career path that I will be pursuing. All in all, the thesis work would not have been completed without keen support of you.

A special gratitude to Dr. Per-Ola Olsson for providing technical assistance during UAV data processing and more than that for your inspiration and valuable suggestions.

I acknowledge the Swedish Infrastructure for Ecosystem Science (SITES) who provided the datasets and the Department of Physical Geography and Ecosystem Science who provided access to the workstation for data processing.

Sincere thanks to all of my friend and faculties of Lund University for making this journey a good one. I am indebted to my colleagues Rojina Shakya, Subash Ghimire, Mihai Patrășcu, Pavlos Aslanis for their moral support, constructive comments, entertainment and caring they provided.

Heartfelt thanks to my lovely family for their immense love, support and encouragement.

1 Introduction

Vegetation phenology describes the various life cycle events that occur throughout the year and has been long identified as a way of studying various processes of an ecosystem (Richardson et al., 2018). For instance, the monitoring of phenology dynamics over the years at various ecological scales helps in understanding how the plants are responding to global change and the way it impacts the forest ecosystems (Klosterman et al., 2017; Park et al., 2019; Berra et al., 2019; Moore et al., 2016).

At the earlier days, plant phenology involved direct human observations of specific phenophase stages (e.g. seedling, flowering, leaf out etc.). Despite such expensive and labor-intensive observation, researchers collected detailed and precise phenological data for a long period of time (Peter et al., 2018; Richardson et al., 2009) at the cost of measurements at a scale of individual species across small geographic areas (Richardson et al., 2006). As a result, the method would be problematic and less reliable in case of generalizing the phenology over regional or global extents based on the series of observations made over few individual species (Richardson et al., 2009). This situation led to the development of new methods that make use of a wide range of sensors.

Modern phenology studies use sensors capable of automatically measuring time series of vegetation at high frequency (Richardson et al., 2013b) from local to the global scale (Klosterman et al., 2014). Satellite based remote sensing has the advantage of evaluating regular patterns of plant cycle at regional and global levels (Eastman et al., 2013; White et al., 2014; Rodriguez-Galiano et al., 2015). However, coarse spatio-temporal resolution associated with satellite observations are insufficient for portraying the spatio-temporal dynamics of vegetation phenology at a larger region (Whiteman and Nemani 2006).

Low-cost high-quality cameras are available making possible to expand the understanding of ecological studies (Brown et al., 2016). An array of imaging sensors often referred to as “*near-surface remote sensing*”, collect data at a high frequency close to the ground to supplement the satellite remote sensing data (Rossi et al., 2019). This ultimately helps to scale up between traditional in-situ observations and satellite monitoring.

Additionally, UAV imagery is capable of generating orthomosaics, by means of photogrammetric techniques, that display vegetation canopy from both nadir and off-nadir positions. This view permits the identification and analysis of a larger number of individual species and area than through phenocameras. Several studies have found good agreement between satellite based remote sensing and phenocameras based on different greenness indices (Liu et al., 2017; Richardson et al., 2018; Cui et al., 2019). However, there is very little research comparing phenocamera RGB-based vegetation indices to UAV-derived Normalized Difference Vegetation Index (NDVI), especially in the case of evergreen forests. Comparing these two datasets may provide insight on the reliability of UAV-derived NDVI, the capability of phenocamera to monitor seasonal dynamics, the combination of results from these platforms together with spectral sensors' data, and the causes of potential differences, similarities and limitations of each indices and platforms.

2 Aim

This study aims to evaluate the ability of UAV and phenocamera data for tracking all-year phenology pattern in an experimental spruce forest, with special focus on spring and fall seasons, using visual inspection data for validation. The study will observe the annual seasonality parameters i.e. Start Of Spring (SOS), End Of Spring (EOS), Start Of Fall (SOF) and End Of Fall (EOF) obtained from both platforms taken over a common region of interest, with the prime aim to investigate the following research questions:

- 1) How accurately does UAV-derived NDVI represent the spectral sensor-based NDVI measurements?
- 2) Which color indices: Green Chromatic Coordinate (GCC), Excess Green Index (ExG) and Normalized Difference of Green and Red (VIgreen) do represent best the NDVI trajectories from UAV and the spectral sensor?
- 3) Is there any variability in the Vegetation Indices (VIs) trajectories among multiple Regions of Interests (ROIs) i.e. (horizon, individual tree canopy) and across the annual time series, extracted from phenocamera images?
- 4) Is there any agreement between phenology phases (start and end of season) derived from phenocamera and UAV datasets?

3 Background

3.1 Remote sensing of vegetation phenology

Land surface phenology is defined as the science which studies the transition of seasonal pattern in vegetated land surfaces using remote sensing techniques. The study of canopy phenology of vegetation during the last decade was based on remote sensing observations from field plots to regional and global scale. Images captured by different sensors store Red (R), Green (G), Blue (B) and/or Near Infrared (NIR) radiance, depending on the sensor type. In order to differ the status of vegetation from images, different metrics are used. The most common metric is called “*reflectance*”, for a specific wavelength band of electromagnetic radiation. Reflectance is used to compute vegetation indices (VIs) such as NIR-visible indices, such as NDVI, or Enhanced Vegetation Index (EVI).

Out of these aforementioned VIs, NDVI is one of the most widely used in phenology mainly due to its robustness against noise, but more importantly, the availability of longer time series data (White and Nemani, 2006; Heumann et al., 2007). Similarly, EVI is the second most extensively used index for monitoring and mapping vegetation phenology at global scale (Zhang et al., 2006). The relationships of these indices with biophysical variables are mainly based on the empirical analysis of measured or modelled data (Jin and Eklundh, 2014). Examples of relationship of VIs against such variables are well explained in Tucker, (1979), where NDVI was found to be correlated to biomass and, similarly, ExG was found to be significantly correlated with Gross Primary Product (GPP, Richardson et al., 2009). Many studies (e.g. Liu et al., 2017; Li et al., 2019; Cui et al., 2019; Keirith et al., 2019) have successfully revealed how time series of such VIs can be effectively used to keep track of change in vegetation and eventually extract the phenological transition dates.

3.2 Near-surface remote sensing derived phenology

The onset of satellite-based remote sensing created unique opportunities in the field of monitoring changes in spectral characteristics of different vegetation types globally. However, global scale phenology monitoring technology, despite having many benefits, are confined by the coarse spatio-temporal resolution, cloud coverage, uncertain atmospheric corrections and by the lack of sufficient ground validation data

(Keenan et al., 2014a). Recent technological development of automated near-surface remote sensing techniques act as a bridge between visual in-situ observations and large scale remote sensing products (Richardson et al., 2013b). This approach involves the use of radiometric/imaging sensors mounted on a vertical elevated structure (e.g. steel towers, buildings or poles) which record and estimate the change in vegetation at a spatial scale equivalent to visual human inspection.

The reasons behind considering near-surface remote sensing as one of the potential methods for routinely monitoring of phenology as per Richardson et al., (2013b) are: (a) the possibility to focus on individual species (spatial scale $\approx 1 - 100$ m) (b) continuous data acquisition (data frequency between several minutes to an hour), (c) the capacity of generating both quantitative (time series of seasonal greenness) or categorical metrics (specific phenodates based on visual inspection), and (d) relatively cheaper than other available techniques. The sensors are usually mounted on a tower at a height equivalent to capture the canopy reflectance at a very high temporal resolution.

Near-surface remote sensing technologies can be categorized as radiometric sensors and imaging sensors. Radiometric sensors measure the incoming radiation reflected from the canopy in specific regions of electromagnetic spectrum while, the imaging sensors (Figure 1) capture digital images in RGB or multi-channel systems (Richardson et al., 2013b). The RGB information of the vegetation can be extracted by using simple image processing methods to calculate a non-NDVI based indices of plant greenness. A common index of greenness from such RGB images is called Green Chromatic Coordinate (GCC, Toomey et al., 2015; Berra et al., 2019). In addition, Excess Green Index (ExG) and Normalized Difference of Green & Red (VIgreen) are commonly used to correlate index values to phenology (Ahrends et al., 2009; Richardson et al., 2007; Sonnentag et al., 2012; Zhao et al., 2012). The GCC and ExG are developed as a measure of vegetation greenness to overall image brightness (Gillespie et al., 1987), while the VIgreen uses the visual Green band in place of near-infrared in NDVI formula (Rouse et al., 1974). Many studies have successfully revealed that the phenophase transition dates are computed from digital images acquired by imaging sensors and have well correlated with plant cycle events of spring budburst and autumn senescence (Toomey et al., 2015; Klosterman et al., 2018; Keenan et al., 2014a; Richardson et al., 2017). The time series of different VIs derived from phenocamera imagery have been

previously utilized for evaluating satellite-based phenology products, and at the same time, to get an idea on how canopy phenology relates with ecosystem processes (Elmore et al., 2012; Toomey et al., 2015).

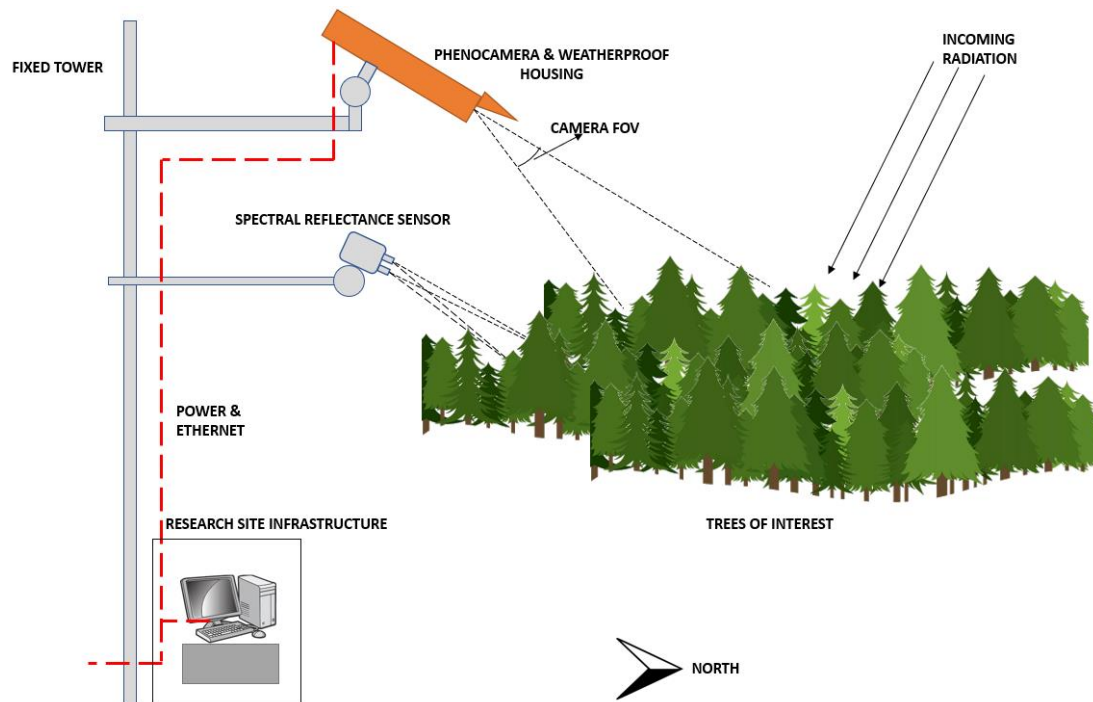


Figure 1. Schematic diagram of a generic phenocamera deployment plan at a forested research site. The camera is placed on a tower taller than the vegetation, with a field of view (FOV) across the landscape oriented towards north to minimize lens flare and, shadows. A spectral reflectance sensor is also mounted on the tower, which measures NDVI. Images captured by the system are uploaded to the server once a day via internet (modified after Richardson et al., 2013b).

3.3 UAV remote sensing

Another example of near-surface remote sensing platform alternative to satellite remote sensing is the UAV, which has the capability to tackle some of the problems of satellite-based measurements: for instance, cloud coverage or coarse temporal resolution. UAVs are small, easy to deploy, and inexpensive, making them popular in the geospatial field for various applications. Consumer grade RGB cameras mounted on UAV, in few case studies (Arko and Joshua, 2012; Berra et al., 2017; Rasmussen et al., 2016) demonstrated the reliability of derived vegetation indices. These small unmanned survey vehicles can also carry different sensors such as thermal, multispectral and, hyperspectral cameras (Burkart et al., 2017), making them feasible to explore vegetation parameters such as crop surface models and chlorophyll content (Aasen et al., 2015). A number of studies have already shown the enormous potential of UAV in monitoring the phenology dynamics in various tree species across relatively large forest community (Berra et al., 2019; Klosterman et al., 2017; Park et al., 2019).

UAV datasets have revealed that the time series information from them can successfully extract the complete seasonal trajectories of tree species in a forest community at an individual tree scale, in a similar manner as that of satellites (Berra et al., 2016; Berra et al., 2017; Klosterman and Richardson, 2017). In addition, these studies also suggest that the time series retrieved from UAV images can be a valuable asset in validating satellite-derived phenological products. Despite the success at preliminary stage, a number of challenges yet remain to be solved to generate quality time series information for phenology monitoring. Spatial misalignment of tree crowns extracted from orthophotos derived from different acquisition dates, challenging to effectively decouple understory/overstory canopy phenology due to high spectral variability in forest areas, and lastly the radiometric calibration of UAV imageries are some of the challenges that could hamper the forest phenology monitoring with UAV.

Radiometric calibration of the UAV datasets can be challenging, mainly because of the varying illumination conditions throughout the flights conducted within a year as a means to capture the change in vegetation (Berra et al., 2017). One approach as practiced in Berra et al. (2016) was using static settings throughout flights in a year making it possible for time series comparison. In an article by Burkart et al. (2017), the research was conducted by utilizing reflectance panels in each flight and analyzing the digital numbers (DN) within those panels to check if the digital values were stable over the time. Smith and Milton (1999) proposed empirical line calibration method which is the most popular radiometric calibration method and that has been used in several studies (Berra et al. 2017; Bueren et al. 2015) successfully to both RGB as well as multispectral cameras. This method assumes constant atmospheric effects across the image, no illumination variation in the image and consideration of Lambertian surface. These assumptions can be problematic in case of UAV flights as there is high chances of cloud cover variation during each flight and also the reflectance panels are not truly Lambertian thus exhibiting bi-directional reflectance properties. There exists more radiometric calibration method such as the darkest target method, flat field method and internal mean method (Yang et al., 2017). The process of radiometric calibration differs from study to study and method to method. Hence, the choice of the radiometric calibration method for measuring reflectance need to be adapted in such a way that facilitates to improve the comparison between UAV-derived phenology with the one obtained from satellite, phenocamera or spectral sensor observations.

4 Materials and Methods

4.1 Study Area

The study area (Figure 2) consists of around 900 ha of mixed coniferous forest of spruce, pine and deciduous trees at Asa Experimental Forest Research Station, which is part of the Swedish Infrastructure for Ecosystem Science (SITES) project (<https://www.fieldsites.se/en-GB>). Asa is located 37 km north of Växjö (57°10'N, 14°47'E). For a detailed description of the study area, please see SLU (2020).

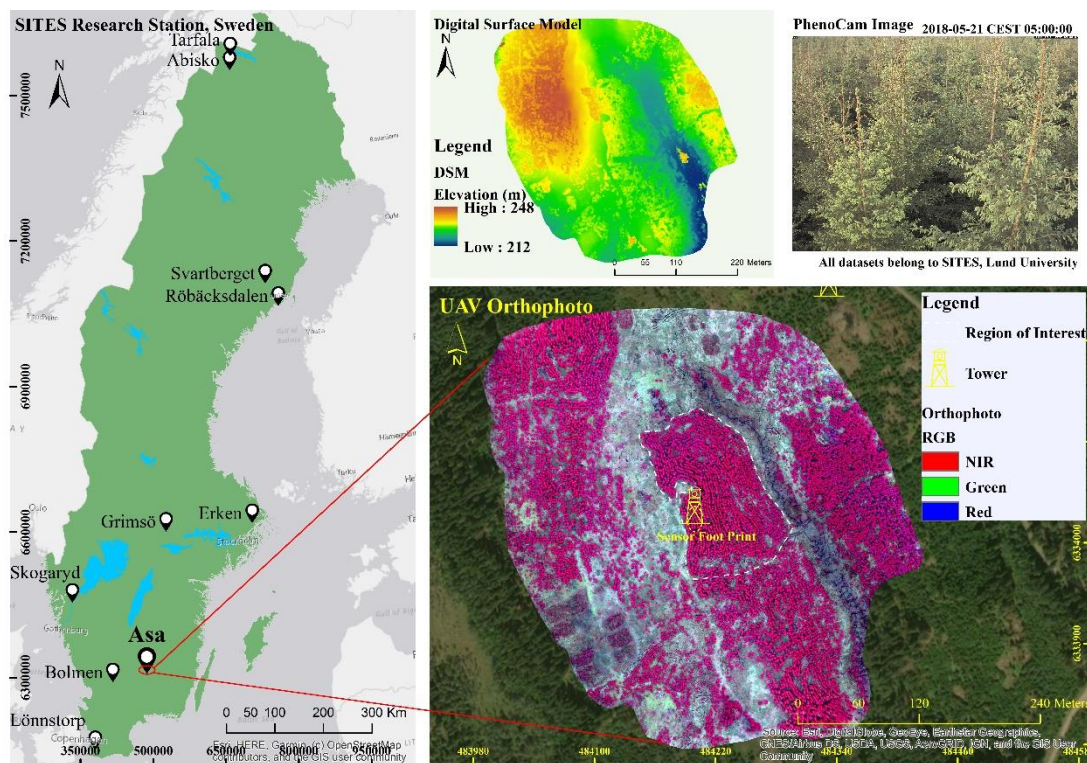


Figure 2. Map showing the location of Asa Research Station, Digital Surface Model (DSM) of the site, UAV Orthomosaic (lower right) and a sample phenocamera image (upper right)

The terrain within the area has flat topography in the south-eastern and western part, while north-western part has relatively elevated area with an altitude of approximately 212 – 240 meters above mean sea level. The reason behind choosing this research station lays on the diversity in terms of tree species and, most significantly, the continuous UAV and phenocamera datasets for both years. In addition, it also offers spectral sensor measurements of NDVI which shall serve for the validation of VIS values obtained through UAV and the phenocamera. For a wide range of ground-based monitoring of vegetation health (e.g., grassland, plant and forest canopies), spectral sensor measures reliable NDVI (see: <http://www.metergroup.com>).

4.2 Datasets

All the datasets used in this research was measured at Asa Experimental Forest Research Station and are collected as the routine observation schedule for research-oriented activities of the station. The station is collecting different data from a wide range of sensors, including phenocamera, UAV, spectral sensors, climate data as well as flux tower measurements.

4.2.1 Phenology Cameras

The study used the data of one phenocamera that is mounted on a tower facing south, at a height of 7 meters above ground level, pointing 45° down from the horizontal, which captures digital imagery of the foreground canopy inside its Field of View (FOV, 45°).

The phenocamera images (for an example: Figure 3) were acquired by a Mobotix 5 MP RGB camera, at a resolution of 2592 × 1944 pixels. The camera captures a colored three-layer red, green and blue image. The images for the year 2018 and 2019 were downloaded from the SITES project server. All the images were captured at hourly temporal resolution between 5 a.m to 8 p.m. There were altogether 5754 images for the year 2018, whereas the year 2019 had only 3446 images (only up to August 4th, after which the data transfer stopped due to hardware problems).



Figure 3. Sample Phenocamera image captured on 05/24/2019 (Source: SITES)

4.2.2 UAV

The UAV flights were conducted using a Parrot Sequoia multispectral camera, for more information, please see (Parrot SEQUOIA+, 2020) on board of a rotary wing aircraft named 3DR SOLO, for detailed description, please visit (3DR Solo Drone Review, 2020). The hardware and operational specifications associated with this UAV are mentioned in the Table 1.

Table 1. Detailed specifications of UAV system. The UAV system was a quadcopter with flight endurance upto 25 minutes at 1.2 kg take-off weight.

<u>Hardware Specifications</u>	
Type	Multi-rotor
No. of rotors	4
Propeller size	25 cm × 11.4 cm
Body Material	Carbon fiber
Dimension	Height: 25 cm; Motor-Motor dimension: 26 cm
Self weight	1.5 kg
Suggested Payload	0.5 kg
Camera System	Parrot Sequoia
Battery capacity	Lithium polymer, 5200 mAh
<u>Operational Specifications</u>	
Area coverage	Approx. 7 ha (Dependent on flying height & battery)
Flight time	Approx. 25 min (based on weight & wind condition)
Flight mode	Manual & Autonomous
Flying height	Approx. 100m (can be adjusted before flight)
Automatic Flight Planning	Yes
Maximum horizontal speed	25.5 m/s (Average speed during flight: 8 – 12 m/s)
Maximum vertical speed	5 m/s
Frequency	2.4 GHz

The UAV system has the payload capability comprised of Global Positioning System (GPS), accelerometer, compass, and camera system loaded with Parrot Sequoia camera. Despite flights were conducted with both RGB and multispectral cameras on board the UAV, only multispectral images were used in this research.

The multispectral camera used in the flight was the four spectral bands Parrot Sequoia. The camera is designed to acquire images in several spectral bands: G, R, Red Edge (RE) and NIR, with central wavelength at 550, 660, 735, and 790 nanometers (nm), respectively. The bandwidth is 40 nm for G, R and NIR and 10 nm for RE. The multispectral sensor was installed under the drone facing the forest canopy. The images were captured by 1.2 MP monochrome sensors at a resolution of 1280 × 960 pixels in raw format and later saved as .tif file. Figure 4 (left) depicts the picture of multispectral sensor.



Figure 4. Parrot Sequoia multispectral sensor (left) and Sunshine sensor (right), Source: Sequoia manual

The details about the Parrot Sequoia sensor is given in Table 2.

Table 2. Parrot Sequoia Camera Specifications (Source: Parrot Sequoia, User Manual: <http://www.parrot.com>)

Name	Parrot Sequoia
Focal Length (mm)	4.0
HFOV (°)	61.9°
No. of spectral bands	4
Wavelength range (nm)	530 – 810
Dimension (mm)	59 × 41 × 28
Resolution (pixel)	1280 × 960
Bit depth	16
File Format	Raw/TIFF
Weight (g)	72

The flight frequency for the study period was roughly one flight per month starting from April to August for 2018, whereas the following year the images were captured between April to October (Table 3, Appendix A). The flights were not conducted in a fixed interval of time mainly because of weather conditions. The missions were programmed

to fly at a flying height of 80m above ground level with frontal and side overlap of 80%. Most of the flights were conducted at mid-day (between 9 a.m. and 4 p.m.) on either clear days or evenly overcast days. The UAV was pre-programmed to follow the waypoints that would cover up the study area in two flights of approximately 10 minutes each. The camera and image settings were kept identical for all flights, in *auto* mode (i.e. camera chooses shutter speed and ISO value while it has a fixed aperture) for exposure compensation. The incoming radiation data during the missions were measured and recorded by the sunshine sensor mounted on the UAV. The primary purpose of using sunshine sensor was to calibrate the images depending upon the incoming sunlight. The provision of sunshine sensor makes it possible for light normalisation of the photos irrespective of the sunlight variations during image acquisition. The sensor is depicted in Figure 4, right.

Three teflon reflectance panels (see more at: <https://www.labspherestore.com/product-p/as-008xx-x00.htm>), often defined as ground calibration targets (GCTs), and ground control points (GCPs) were placed within the UAV survey's coverage on all image acquisition dates for the purpose of radiometric calibration and georeferencing, respectively. The detailed information on all of the UAV flights carried out during the study period is mentioned in Table 3 (Appendix A).

4.2.3 Spectral Sensor

The spectral sensor used in the research was the NDVI Decagon SRS (Spectral Reflectance Sensor). The SRS-NDVI are two-band radiometers designed to measure the incident and reflected radiation in wavelengths suitable for the computation of NDVI. The SRS-NDVI system is mainly comprised of two types of sensors: (1) the SRS-Ni hemispherical, and (2) the SRS-Nr field-stop lens sensor. The first type is built with a hemispherical 180° FOV looking-up measurements of incident radiation, whereas the second type have FOV confined to 36° for spotting downward to measure reflected radiation from the forest canopy. The two sensors available on SRS-NDVI are depicted in Figure 5.

The SRS-NDVI sensor was mounted on a fixed tower above the canopy of the spruce forest and the measurements were stored on a Campbell CR1000 data logger. Upward and downward-looking sensors measure the incident and reflected canopy radiance,

respectively, every 10 sec at a wavelength band of 650 nm (R) and 810 nm (NIR). Every 10 minutes, the data collected is averaged into a single record.

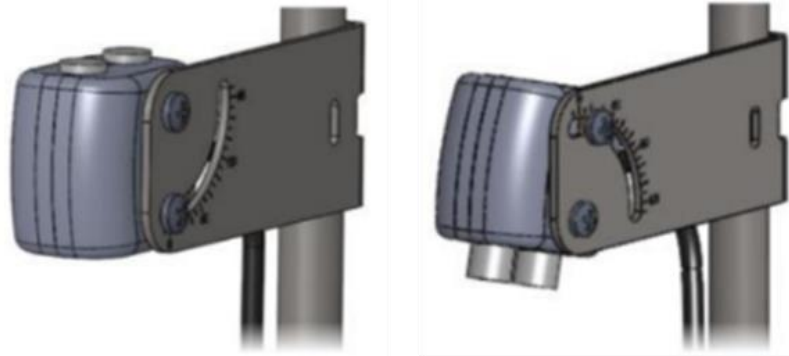


Figure 5. Spectral Reflectance Sensor for NDVI. Cosine corrected hemispherical sensor (left) and Field-stop lens sensor (right). Source: <http://www.metergroup.com>

The footprint of the sensor was computed using the sensor FOV, height and off-nadir angle with a MATLAB software developed at the department by Jin (2011). The same footprint was used to extract NDVI from UAV orthophotos for comparison. The purpose of using the measurements from SRS-NDVI in this study was primarily for the validation of the UAV-derived NDVI. Alongside the validation, the NDVI trajectories obtained from the sensor serve as a valuable dataset for the inter-comparison of visible VIs from the phenocamera to check if the VI trajectories behave in a similar pattern. The specifications associated with the spectral sensors are displayed in Table 4.

Table 4. Measurement specifications of SRS-NDVI sensor

Model Name	SRS-Ni Hemispherical Sensor		SRS-Nr Field Stops Sensor	
	Unit	650nm Spectral Irradiance (R)	810nm Spectral Irradiance (NIR)	650nm Spectral Radiance (R)
Accuracy	5%		5%	
Resolution	$0.0001 \text{ W} \cdot \text{m}^{-2} \cdot \text{nm}^{-1}$		$0.0001 \text{ W} \cdot \text{m}^{-2} \cdot \text{nm}^{-1} \cdot \text{sr}^{-1}$	
Range	0 to $2 \text{ W} \cdot \text{m}^{-2} \cdot \text{nm}^{-1}$		0 to $2 \text{ W} \cdot \text{m}^{-2} \cdot \text{nm}^{-1} \cdot \text{sr}^{-1}$	
FOV	180°		36°	
Dimension	43cm × 42cm × 27cm		43cm × 42cm × 27cm	

4.3 Methods

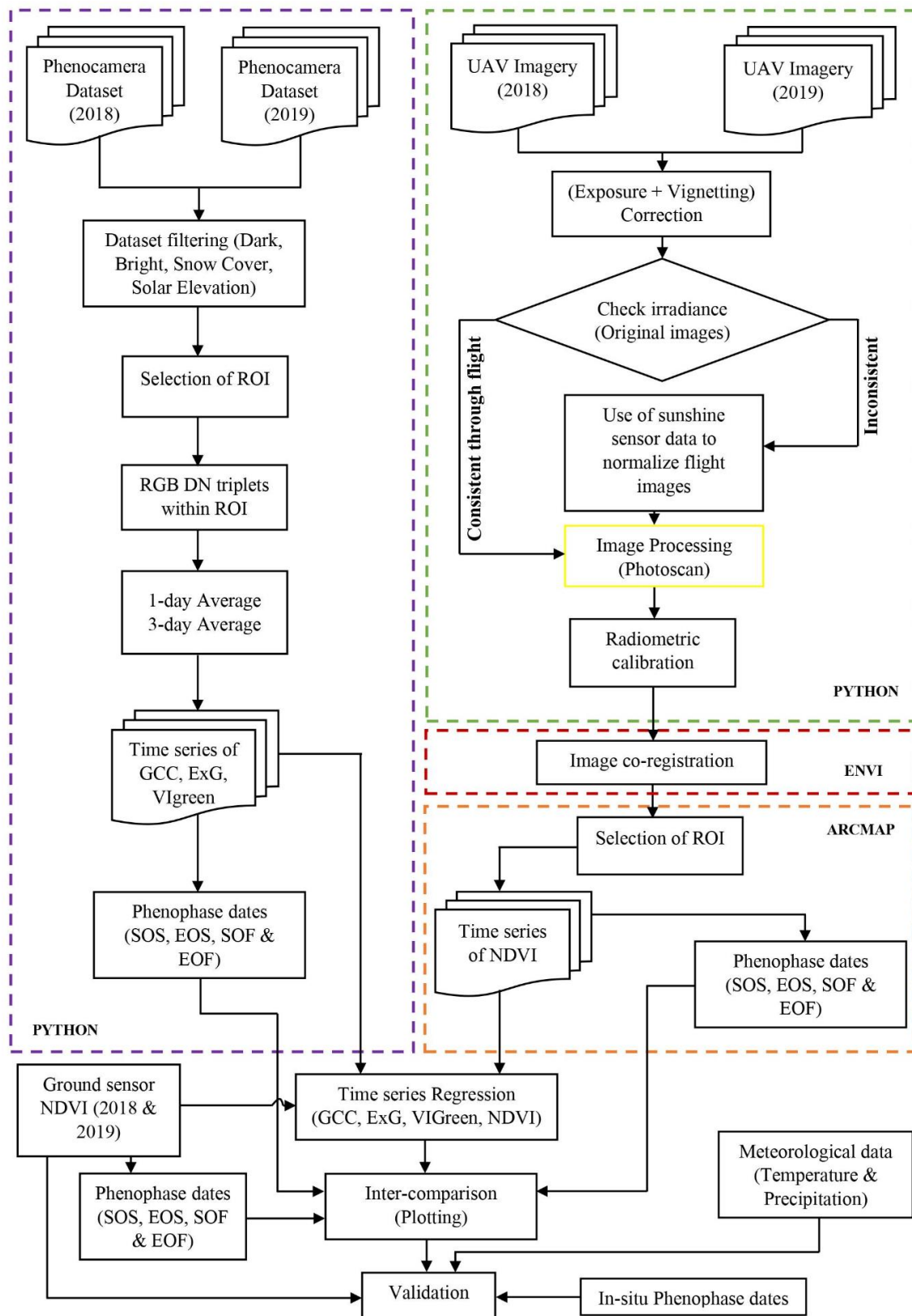


Figure 6. Overall workflow of the research. The workflow is the combined steps of four processing steps to achieve the objective of current research: data collection, data processing, inter-comparison and lastly the validation of those results.

4.3.1 Data Processing

4.3.1.1 Phenocamera Image Processing

The images from the phenocamera in Asa were processed in several steps. First, images with snow and light glare were filtered out manually and then complete dark images (night photos) were filtered out beforehand processing the images. This was achieved by calculating the solar elevation angle, using standard formulas based on Python package ‘*pyephem*’ (<https://rhodesmill.org/pyephem/>), which uses the date and local timestamp information, extracted from the image file name. A threshold of solar elevation angle less than 0° was defined to filter all the completely dark images. All the images with solar elevation angle less than 10° above the horizon (very dark images) and very bright images were excluded at this stage from processing. As per the experiment conducted by Sonntag et al., (2012), the images captured at dawn and dusk that experiences low level of diffused sunlight illumination inclined to have lower VI values compared to those recorded at middle day. Therefore, the very bright (mean $[DN_{red} + DN_{green} + DN_{blue}] > 600$) and very dark images (mean $[DN_{red} + DN_{green} + DN_{blue}] < 100$) were also filtered out on the basis of threshold defined using the total of mean DN across ROIs of all three bands (R, G and B). The images that appeared blurred and had stripes covering more than 90% area of the image were also removed manually. All the images that passed the series of these quality control filters were the valid images from which the time series of vegetation indices were retrieved. Of all valid images, only images between 10 a.m. to 2 p.m. (solar time) were used. The final number of images after these steps were 3222 for 2018 and 2373 for 2019.

In order to extract the vegetation indices, firstly multiple ROIs were defined at a suitable location within each digital image, from which the time series of RGB DN triplets were extracted. The ROIs were constant for all images. An effort was made to confirm that the time series was not affected by the possible camera movement, which would alter the camera Field of View (FOV) and ultimately disturb the integrity of the extracted information. Figure 7 depicts the ROIs selected for the study. The reason behind choosing multiple ROIs was to see if there was variation in time series of VIs. Most of the analysis in this study was based on full phenocamera FOV (ROI #5, white box in Figure 7) except in one particular section where the analysis was made between ROI #1 (red) versus the ROI #4 (green). And this analysis was limited to year 2018 only because in 2019 due to vegetation growth, the ROI #4 could no longer be differentiated.

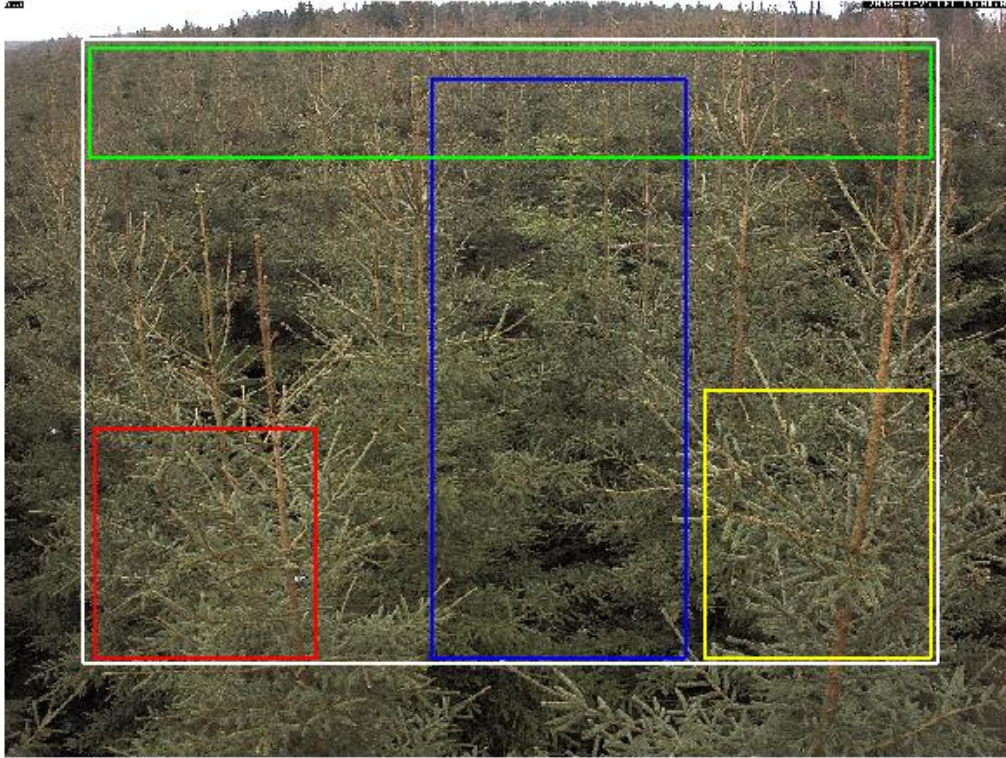


Figure 7. Region of Interest for extracting time series of RGB DN Triplets (each colored rectangle refers to a different ROI). Red and yellow colored rectangles represent ROI that are close to the camera and represent individual spruce tree canopies. The blue one represents a ROI with understory vegetation including shadows, while the green rectangle represents the ROI that is far away from the camera, close to horizon. Finally, the white rectangle represents the dominant FOV of the images. (Image Source: SITES)

The second step of phenocamera data processing was to extract the DN values distributed across all the pixels in the corresponding ROI. A python code written to extract the mean DN values of RGB bands across the defined ROIs. Then, the extracted mean DN values were fed into equations (1), (2) and (3) to evaluate GCC, ExG, and VIgreen, respectively.

$$GCC = \frac{DN_G}{(DN_R + DN_G + DN_B)}, \quad (1)$$

$$ExG = 2 * DN_G - (DN_R + DN_B), \quad (2)$$

$$VIgreen = \frac{(DN_G - DN_R)}{(DN_G + DN_R)}, \quad (3)$$

where DN_R = mean red DN, DN_G = mean green DN and DN_B = mean blue DN for the chosen ROI.

With the calculation of these indices, the impact of variations in scene illumination can be mostly minimized (Toomey et al., 2015; Richardson et al., 2018b; Klosterman et al., 2017; Sonnentag et al., 2012).

The same vegetation indices were calculated over the predefined ROIs with the primary purpose of portraying the seasonal time series of the studied forest canopy. For most of the applications, a very high temporal resolution (e.g. hourly resolution, like in this research) seems unnecessary. This is because, in general, the vegetation color over such short period of time remains relatively constant. With this consideration in mind, we preferred to calculate average of all the valid images for the vegetation indices mentioned above, in three different time aggregations. First, we averaged the DN values of pixels within each ROI for the image corresponding to noon, only. The second approach was the average of DN values within each ROI, calculated from all the valid images within 1-day interval (between 10 a.m. and 2 p.m., solar time), and the last one within 3-day interval, as experimented in Richardson et al. (2018b). Figure 8 shows the output of 1 and 3-day interval computed from the time series of GCC (a, b) for year 2018 (see Appendix B for ExG and VIgreen and Appendix C for all VIs in year 2019).

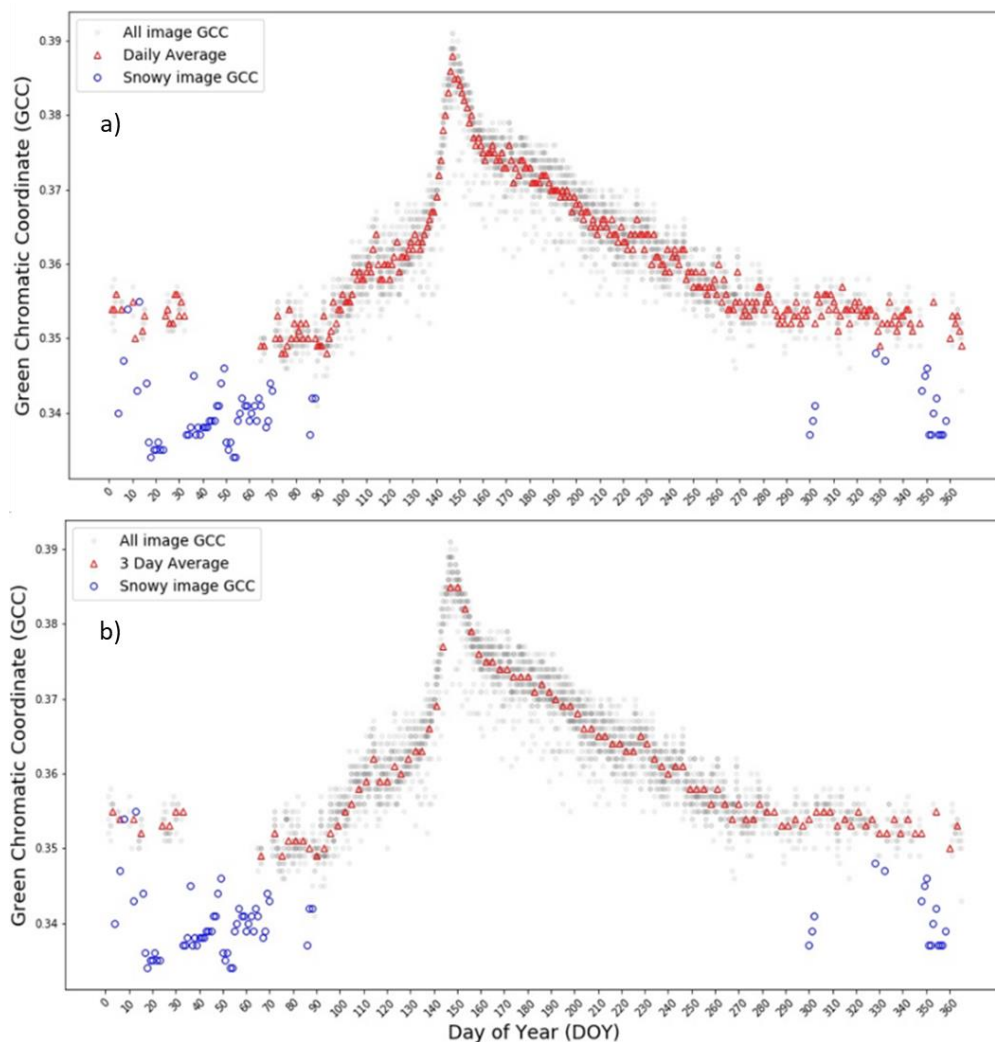


Figure 8. Example time series of phenocamera GCC for defined ROI. Grey circles are all image average GCC (every hour) value within ROI; blue circles are average GCC for snow covered images and red triangles are 1-day (a) and 3-day (b) average GCC values.

The reason behind choosing to explore the 1-day and 3-days average was to decide the level of noise that can be associated to intra-daily images. In case of every 3-day time step, the data appeared to be less noisy (see Figure 8) than the one compared with the daily timestamp. In addition to mean VI values over all the valid images, the 50th, 75th and 90th percentile value across a 3-day moving window were calculated for all VI. However, only 3-day averages were used in the analysis. In addition, by looking into the phenocamera images visually, we collected day of year information when green sprouts appear (SOS) and the day when greenness no longer changes (EOS) in the images which shall serve for the validation of phenophase transition dates from curve fitting.

4.3.1.2 UAV Image Processing

First, the sunshine sensor data from UAV flights were retrieved from the images' metadata and then plotted, to check the incoming light conditions, using a Python code by reading the Exchangeable Image File Format (EXIF) tags for each single band (G, R, RE & NIR). Based on this plot, UAV flight data were characterized in 3 ways: (1) consistent sunny incoming light, (2) consistent cloudy incoming light, with slight variation, and (3) complex incoming light recorded during the mission. The three different cases are depicted as a, b and c in Figure 9 below:

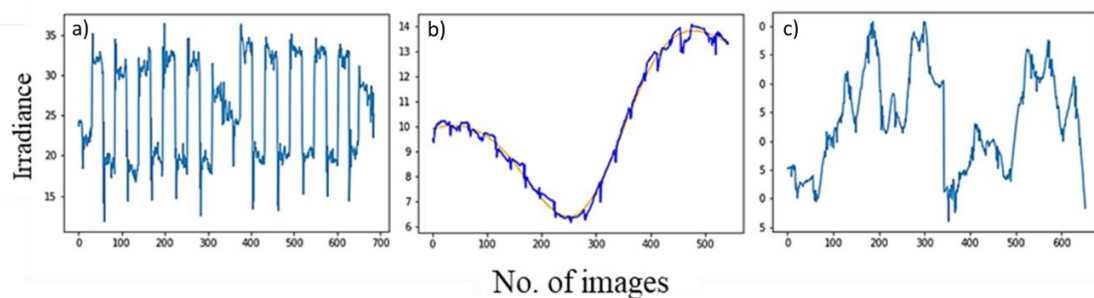


Figure 9. Sunshine sensor data plot showing variation of irradiance within UAV mission

The UAV flights that presented irregular and complex light variability during the flight (3) (Figure 9, c) were discarded. The data that presented constant light, under sunny (1) (Figure 9, a) or overcast sky (2) (Figure 9, b), were further processed. The information regarding the flights that were accepted and rejected for further processing are listed in Table 3 (Appendix A).

After filtering out the flights, the images were ready for the second level of processing. This included the exposure and vignetting effect correction of all flight images.

Exposure is simply about how dark or light image will appear, while vignetting is defined as a rate of falloff in illumination strength that relies on the angle of incoming radiance (Arko and Joshua, 2012). The flight data showing the consistent irradiance throughout the mission (1) was processed only for the exposure and vignetting correction before feeding into Photoscan Metashape 1.4.2 (Agisoft, St. Petersburg, Russia) for image processing. Similarly, the flight data that showed variation in irradiance data that could be handled by normalizing for incoming light condition from sunshine sensor data (2) were normalized using a polynomial trend of degree 'n' or spline trend, based on the nature of the data, in Python. The degree of polynomial was chosen in such a way that it fits the irradiance data with coherence at the start and end of each flight. This is because the mission captured the GCT images only at the beginning and end of the mission, which were later used for radiometric calibration of the derived orthophotos.

The methods for minimizing vignetting effect was based on the use of vignetting polynomial which are provided in the image metadata called XMP (Extensible Metadata Platform). XMP allows the camera manufacturer to add metadata other than standard EXIF (Exchangeable Image File Format) tags. This XMP metadata was used for the generation of a correction factor on a pixel by pixel basis, which is simpler to compute and more accurate (Wonpil, 2004). All the process of exposure compensation, vignetting effect correction and normalization of the images were carried out using the Python and Geospatial Abstraction Data Library (GDAL, for more information please visit, <https://gdal.org/>) was used to save images after all corrections. The python codes for all these three processes were developed at the department and were allowed to use in this study.

All the flight images that had undergone the process of these corrections were thereafter imported into Photoscan photogrammetry software package for image processing. Figure 10 shows the workflow for generating the orthomosaics from the imported imageries of each flight.

The parameter settings used in Agisoft at each step mentioned in the workflow are:

1. **Align Photos:** - Accuracy: High; Pair selection: Ground control; Point limit: 40000; Constrain features by mask: No.
2. **Build Dense Point Cloud:** - Quality: High; Depth filtering: Aggressive; Reuse depth maps: No.

3. **Build Mesh:** - Surface type: Arbitrary; Source data: Dense cloud; Interpolation: Enabled; Face count: High.

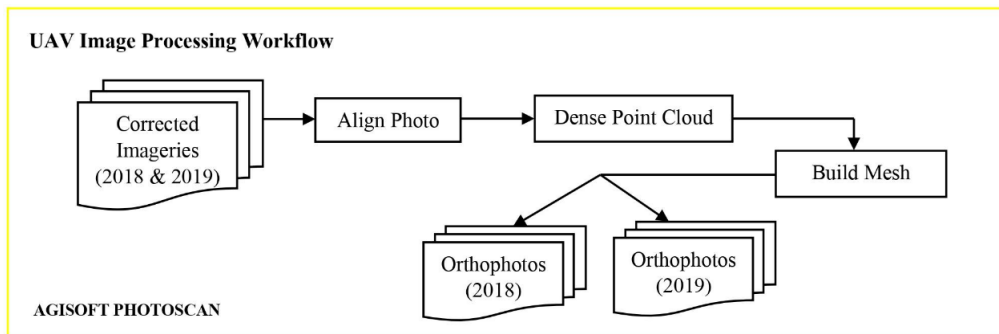


Figure 10. Image processing workflow in Photoscan for generating Orthophotos

A significant amount of pixel reached the top of the spectral range (saturated pixels) in the images of each flight, mostly in the G band and least in the NIR band when exposing. To get a balanced exposure of the entire images, some of the brighter pixels gets overexposed. Photoscan Metashape cannot handle them. As, these saturated pixels influence the reflectance values, therefore, they were masked out using GDAL Python and the mask files were saved in TIFF format. Photoscan allowed to import these masks, which were used in the step of orthophoto generation, to remove the saturated pixels. While creating the orthophotos, the blending mode was deactivated in order to preserve the original DN values (Berra et al., 2017). Five Ground Control Points (GCPs) were used to produce georeferenced orthophoto with spatial resolution of approx. 0.07 m. Three GCP markers were used as check points, which resulted on a root mean square error (RMSE) of ~0.02 m. Only one orthophoto for each study period was georeferenced and used as a reference to co-register the rest of orthomosaics (16 in total; 8 for each year). An instance of complete orthomosaic image is depicted in Figure 11 below:

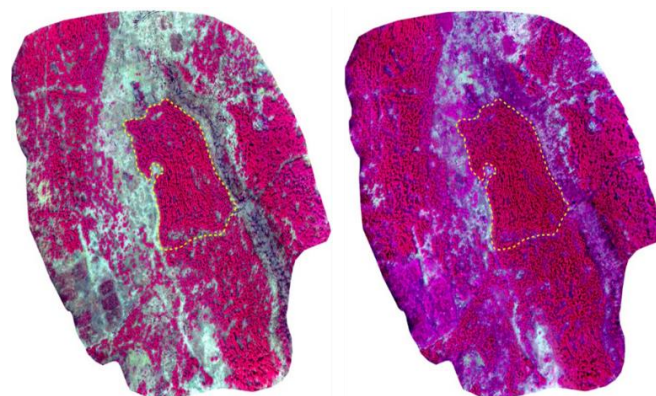


Figure 11. UAV orthomosaic of the study area. One orthomosaic (left) is from 16th April, 2018 and the other (right) is from 26th April, 2019. Yellow dashed polygon represents the main experimental forest area.

Finally, the orthophotos were subjected to radiometric calibration using the empirical line method suggested by Smith and Milton (1999), which is the most widely used method in the remote sensing community. The method relies in mean DN values of three reflectance panels present in the images and their standard reflectance values. The three panels used in the research were black, grey and white referring to 5%, 20% and 50% reflectance. The standard reflectance value of these panels, together with the mean DN of the same panel extracted from a set of images, were used to convert the orthophoto into reflectance, by establishing a linear relationship between those measurements. The study area was covered by the UAV in two separate flights because of limitation in battery, having images of reflectance panels at the start and end of both missions. Because of this, it was required to select the suitable images for radiometric calibration. So, as a part of this calibration, an experiment was conducted to check if there is an effective way of selecting the best image for the calibration. Images of reflectance panels were selected for each flight captured at the start and end and mean DN values for the panels were extracted and analysed. From the experiment, it was realized that the DN values over the panels were mainly affected by 3 parameters: (1) flight height of UAV during image acquisition of panels, (2) position of reflectance panels on the image, and (3) sensor temperature when camera triggered the image.

It was observed that the flight height of UAV while capturing the image of panels have an influence on the pixel values. The images captured close to the flight height of the main UAV missions were selected as a way to cope with this situation. Second, the images with reflectance panel positioned at the centre were found to have less variation in DN values due to small or no influence of solar angles, compared to the edge pixels. Lastly, the sensor temperature for all images were taken into consideration, while selecting images for extracting mean DN values for the radiometric calibration. Most of the flights showed that the sensor was not warmed up enough at the start of mission (e.g., data from one flight in Figure 12), so images with reflectance panels at the end of the mission was preferred for the radiometric correction. However, if the sensor temperature was close to saturation when the first panel images were captured, the images from both start and end of mission were selected for the radiometric calibration.

The extracted mean DN values from the selected images were averaged for each band and later used in the radiometric correction process.

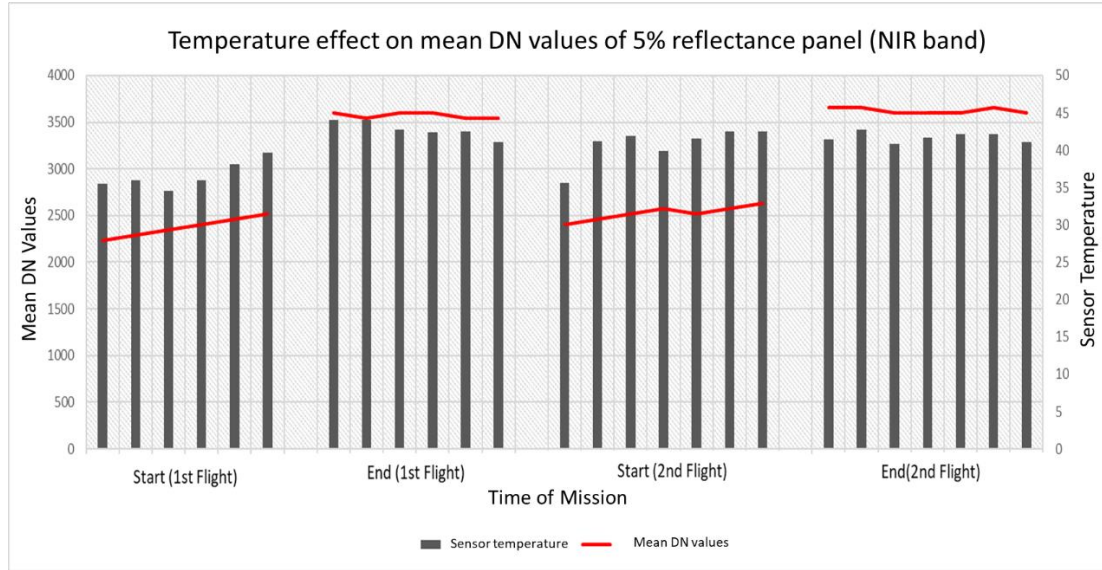


Figure 12. Variation of mean DN values at different stages of UAV mission in relation with sensor temperature. Note that mean DN values plotted here refers to only 5% reflectance panel on NIR band

The images of each flight were calibrated with the images containing reflectance panels carried out during the same flight, to accommodate for the exactly similar illumination conditions.

The radiometrically corrected orthophotos were then used to compute NDVI map of all flights. NDVI is functional variant of simple ratio ($\frac{\rho_{NIR}}{\rho_{RED}}$), with a dynamic range of -1 to +1 (Chuvieco, 2016) and is expressed in Equation (4):

$$NDVI = \frac{\rho_{NIR} - \rho_{RED}}{\rho_{NIR} + \rho_{RED}}, \quad (4)$$

where ρ_{NIR} = near-infrared reflectance, ρ_{RED} = visual red reflectance. The values around 0 represent bare soil and values of 1 refers to vigorous vegetation.

The footprint of spectral sensor was approximately overlaid on top of orthophotos and average NDVI values within it was extracted from each NDVI maps of the study period. The NDVI values were finally compared against the VIs generated from phenocamera and also validated with the NDVI values from the spectral sensor. An instance of NDVI map for two of the flights are depicted in the following Figure 13.

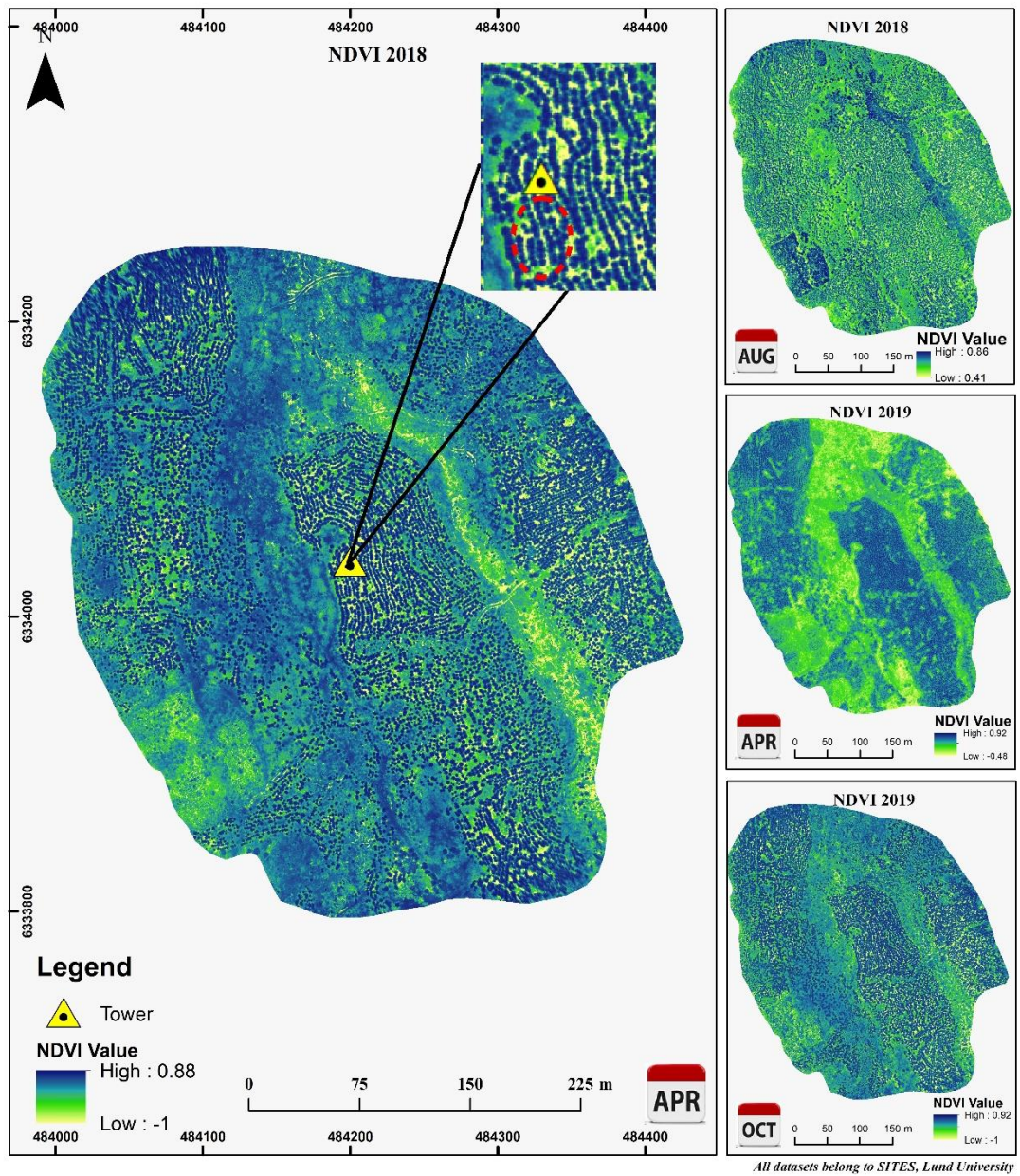


Figure 13. NDVI maps for the year 2018 & 2019. Dashed ellipse (red) refers to the spectral sensor footprint.

4.3.1.3 Spectral Sensor Data Processing

The spectral sensor data was available for each year with irradiance and radiance measurements made by upward and downward looking sensors, respectively. The radiance and irradiance for both red and NIR band averaged every 10 minutes was collected. A subset of measurements was extracted from the full time series, which covered exactly between the same hours and days than the period used for the phenocamera, using a Python code. The calculation of spectral sensor NDVI was done

on reflectance, calculated as a ratio from incoming and reflected radiation, by dividing the downward-looking sensor data by the upward-looking sensor data. The computed reflectance values allowed plotting the NDVI trajectories for both years 2018 and 2019. The data was averaged in similar time aggregates than for the phenocamera, i.e. daily averaged and 3-day averaged NDVI values, and plotted on top of all NDVI values. In addition, the footprint of the spectral sensor was calculated and projected on the ground (see red dashed ellipse, Figure 13). Figure 14 shows the measured NDVI values from spectral sensor with 3-day average values on it.

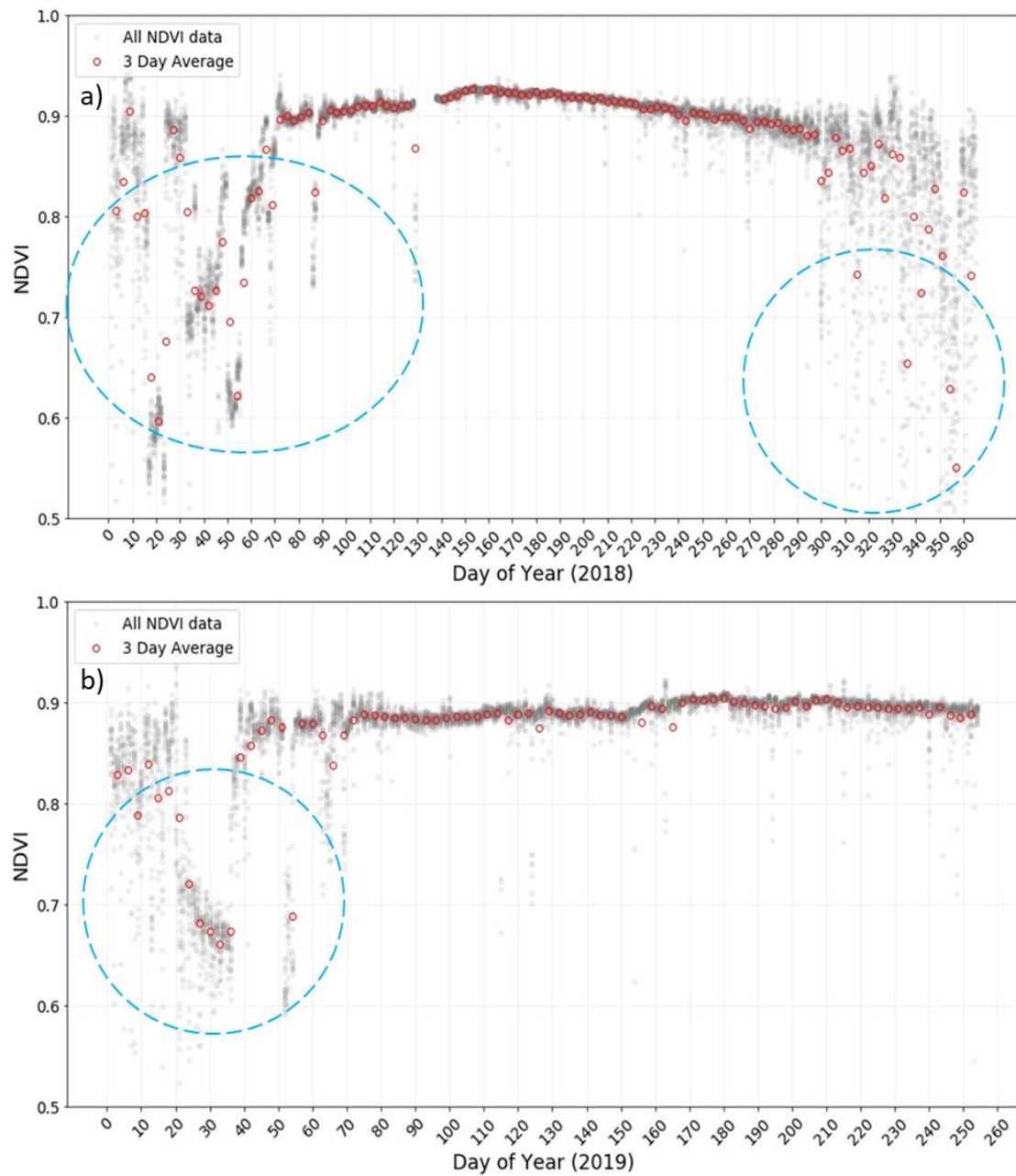


Figure 14. Plot of NDVI measurements from spectral sensor for year 2018 (a) and 2019 (b). Grey dots represent all the NDVI values between 10 a.m.- 2 p.m. while hollow circle symbol (red) represents the average NDVI values every 3 day over the study period. Red circle within dashed ellipse represent NDVI values on snowy day which were avoided from the analysis.

4.3.1.4 Phenology dates from time series data

The time series data obtained from different platforms (UAV, phenocamera and spectral sensor) were further treated with Savitzky-Golay filter (Chen et al. 2004) to remove the residual irregular changes of VI values in the annual cycle prior to estimating phenology dates from it. This process was performed using a first-degree polynomial within a window size of 3 (in the case of UAV-derived NDVI time series) and 5 (in case of the phenocamera VI time series and spectral sensor NDVI time series).

Of all the different curve fitting methods explained in Klosterman et al. (2014), sigmoid functions with double logistic model (Li et al., 2019) were used to fit the time series of phenocamera and spectral sensor VI data, while a spline interpolation method (Richardson et al., 2018b; Klosterman et al., 2014) was used for UAV-NDVI data. The idea behind fitting the curve is to extract the phenophase transition dates from it. The double logistic model applied in the research comprises two sigmoid curves, expressed in *Equation (5)*:

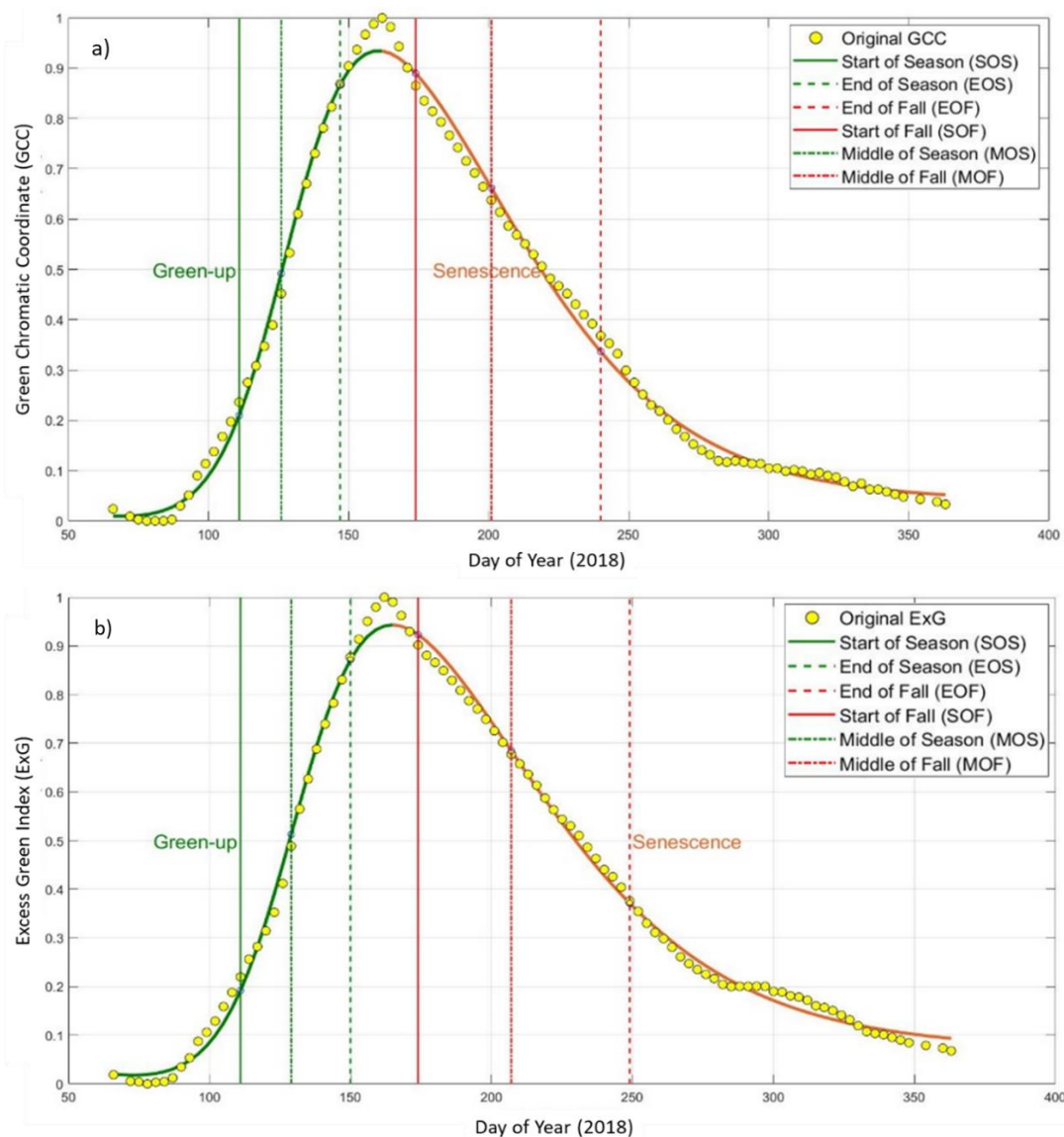
$$f(t) = v_1 + v_2 \left(\frac{1}{1+e^{-m_1(t-n_1)}} - \frac{1}{1+e^{-m_2(t-n_2)}} \right), \quad (5)$$

where, $f(t)$ is the fitted vegetation index value at the day t ; v_1 and v_2 are the background and amplitude of vegetation index over entire year, respectively. The pair parameters m_1 and n_1 in the first sigmoid ($\frac{1}{1+e^{-m_1(t-n_1)}}$) represents the green-up phase of plant growth, while the parameters m_2 and n_2 in the second sigmoid ($\frac{1}{1+e^{-m_2(t-n_2)}}$) records the senescence phase of the vegetation growth. In more specific terms, n_1 and n_2 reflect dates with maximum increasing and decreasing rates of the two phases in sigmoid curves. In a similar fashion, m_1 and m_2 refer to the slopes that plays an important role in deciding the shape of sigmoid curves. These parameters ($v_1, v_2, m_1, n_1, m_2, n_2$) in the double logistic function are the curve fit parameters, which were estimated using the Levenberg-Marquardt technique (Zhang et al., 2004) in Matlab.

The phenology transition dates estimation was based on the fitted sigmoid curves, which were calculated based on the rate of change in curvature (Zhang et al., 2003). The rate of change in curvature (k) is defined in *Equation (6)* as:

$$k = \frac{f''(t)}{(1+(f'(t))^2)^{3/2}}, \quad (6)$$

The phenological transition dates for green-up phase correspond to the three-local extreme in the rate of change in curvature. These first three extreme values in the curvature change rate were the phenological transition dates start, middle and end of spring season (abbreviated as SOS, MOS and, EOS) as proposed by Zhang et al. (2006). These three extremes agree with the 10, 50, and 90% of amplitude in spring green-up phase of vegetation growth (Klosterman et al., 2014). The similar approach was adopted for identifying the start, middle and, end of fall season (defined as SOF, MOF, and EOF) in the senescence phase. No statistical method was used in order to quantify the uncertainty in estimates of transition dates, beside cross validating with phenological transition dates from visual inspection. One instance of the double logistic fit over the time series data (2018) and phenological transition date estimation using the concept of curvature rate change is shown below, in Figure 15, for all VIs from the phenocamera. Consider appendix D for similar fit over time series data of the year 2019.



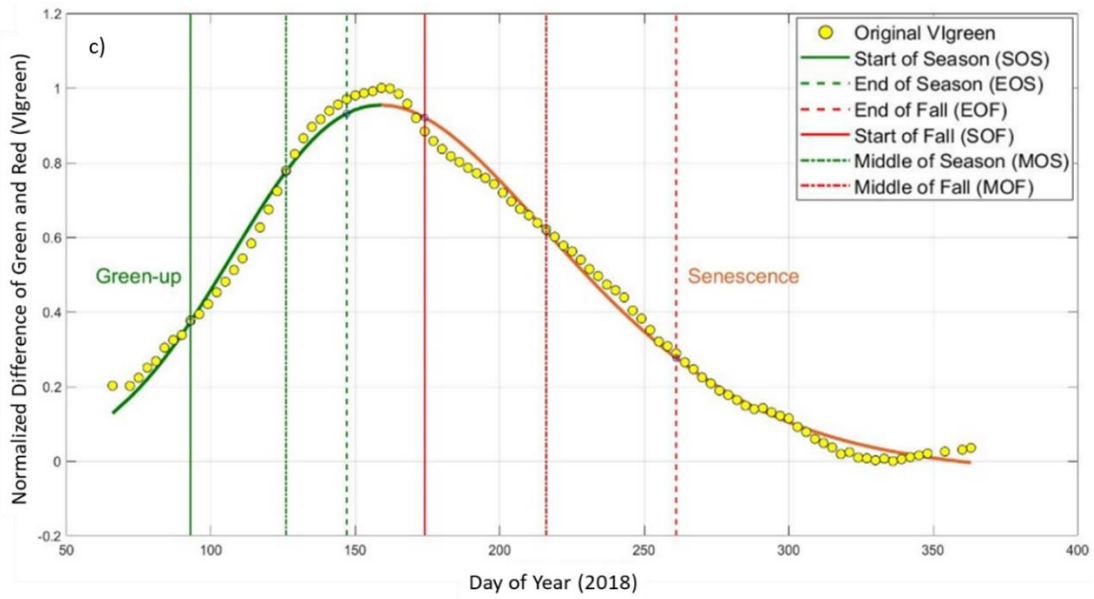
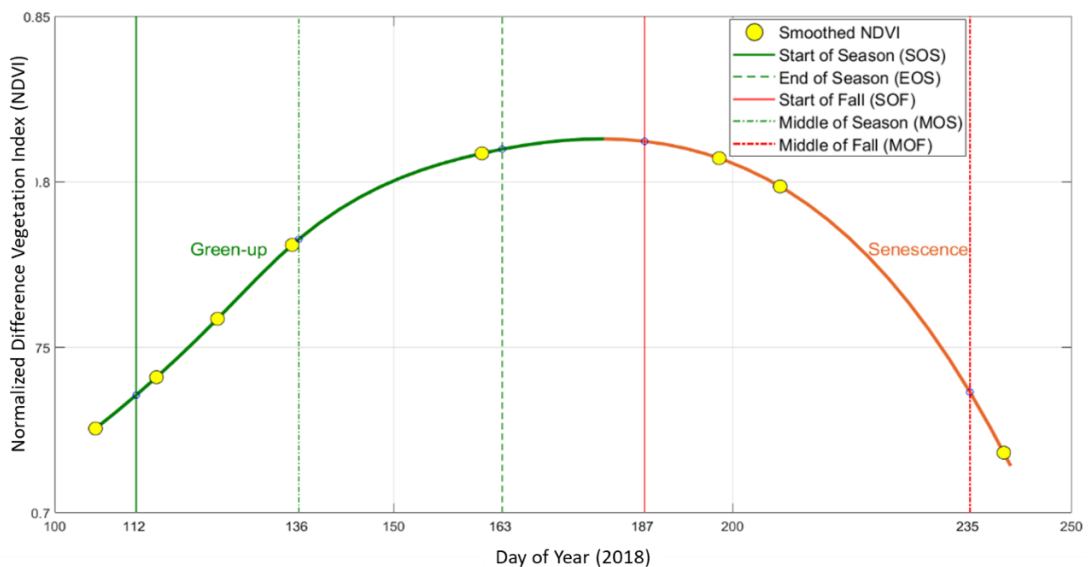


Figure 15. Double logistic fit of 3-day averaged time series of GCC (a), ExG (b), VIgreen (c) and retrieval of phenological transition date from the fit. Green (solid, dashed dot, dashed) lines represent SOS, MOS & EOS while red (solid, dashed dot, dashed) lines represent SOF, MOF and EOF events respectively.

In case of the UAV-NDVI time series, there were fewer data (only eight NDVI values for 2018 and seven values for 2019), for which the double logistic model was not able to fit the curve suitably. The spline interpolation technique resulted in a better fit and eventually led to more accurate phenological transition dates. The calculation of phenological transition dates for spring and fall from UAV-derived NDVI time series was the same method than for the double logistic curves, used for spectral sensor and phenocamera data. Figure 16 shows the result of spline interpolation fit to the UAV-derived NDVI data and the phenological transition date estimations from the fit.



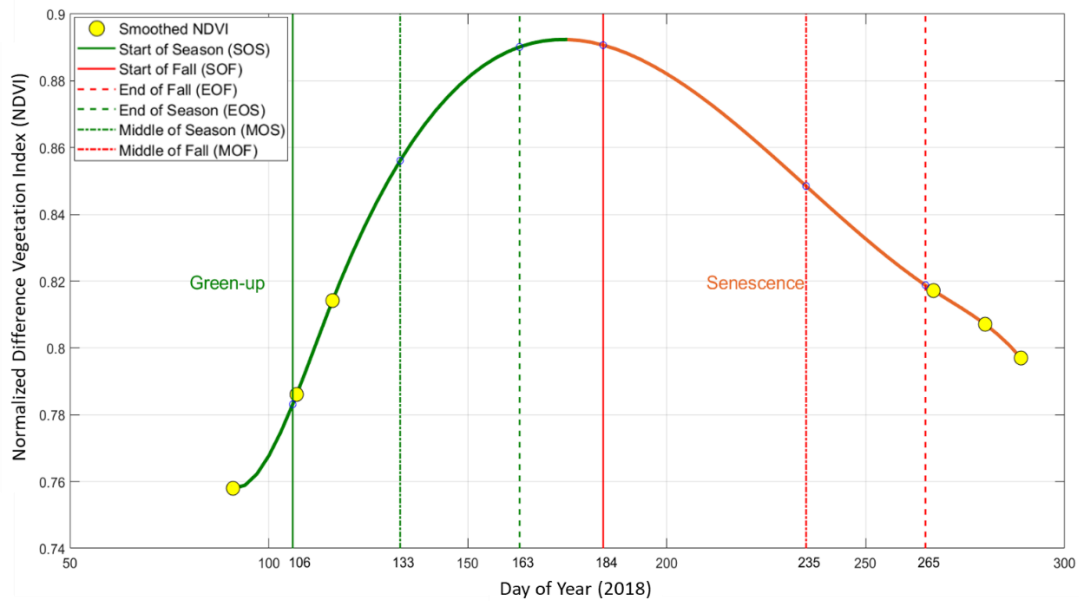


Figure 16. Spline interpolation fit of UAV-derived NDVI time series and retrieval of phenological transition date from the fit. Green (solid, dashed dot, dashed) lines represent SOS, MOS and EOS, while red (solid, dashed dot, dashed) lines represent SOF, MOF and EOF events, respectively. Upper plot and lower plot represent 2018 and 2019, respectively.

4.3.2 Inter-comparison and validation

The time series data and phenophase transition dates from the studied platform was analyzed in two levels: (1) compare VI values from different sensors, and (2) evaluate the accuracy in estimating transition dates of all sensors, comparing it with the visual inspection data. Since, the time series of VIs from different sensors are in different units and scale, so to facilitate the comparison, the three phenocamera-based vegetation indices and spectral sensor were normalized by using the process of min-max normalization as a means to match all the values to be in the range of 0 – 1. The NDVI data from spectral sensor was considered to be the most reliable time series data, and therefore used as a reference in comparing and validating the time series from rest of the sensors while the visually inspected phenophase transition dates were used to validate the transition dates from different sensors. The comparison and validation were done using RMSE and Pearson’s correlation coefficient. The RMSE and correlation coefficients were evaluated between UAV-NDVI and spectral sensor NDVI, phenocamera VIs versus the UAV-NDVI, and also between phenocamera-based VIs and spectral sensor NDVI. The calculation of RMSE and correlation coefficients in case of UAV-NDVI against spectral sensor NDVI and phenocamera VIs versus UAV-NDVI, included identical date (e.g., April 3rd 2018, and April 3rd 2019) VI values, while

for phenocamera VIs against spectral sensor NDVI, it included the complete annual time series data.

For the comparison of phenophase transition dates, visually inspected SOS and EOS data from phenocamera images were considered as reference. SOS was defined when the green sprouts started to be visible on the image, while EOS was defined when sprouts fully develop and no longer differentiate with rest of the leaves. However, it was not possible to define the dates for other seasonality events as the studied forest was evergreen and the changes in vegetation could not be differentiated with human eyes. The agreement between the phenophase dates from all sensors were compared against each other, and finally validated to visual inspection data. This comparison led to compute the bias in terms of number of days, which give clear reflection on which applied methods give close approximation to visually assessed dates.

All the stated python codes that are written as a part of this research are available in <https://github.com/shangharsha2929/ASA.git>.

5 Result

5.1 Comparison of UAV and Spectral Sensor-derived NDVI

The computation of Pearson's correlation coefficient revealed the agreement between the UAV and spectral sensor-derived NDVI values. The agreement between them was reflected by a positive, strong correlation ($r > 0.75$, Table 5). The extracted UAV-NDVI values of all flights from 2019 was observed to have slightly higher correlation coefficient (RMSE: 0.040; $r = 0.903$) compared to 2018 (RMSE: 0.149; $r = 0.780$) as shown in Table 5.

Table 5. Pearson's correlation coefficient between UAV-NDVI and spectral sensor NDVI for the years 2018 and 2019

Year	Spectral sensor NDVI Vs. UAV-NDVI			Spectral sensor NDVI Vs. Spline fitted UAV-NDVI		
	No. of Samples (N)	Correlation Coefficient (r)	RMSE	No. of Samples (N)	Correlation Coefficient (r)	RMSE
2018	8	0.78*	0.149	42	0.92**	0.104
2019	5	0.903*	0.04	52	0.94**	0.016

* and ** indicates significance level value less than 0.05 and 0.001 respectively.

The graphical plot showing raw UAV-NDVI compared against spectral sensor NDVI together with smoothed UAV-NDVI is depicted in Figure 17.

Based on the plot (Figure 17 and Appendix E), the UAV-NDVI values for the year 2018 (top) seems to be following the spectral sensor-based NDVI trajectories by maintaining more or less constant offset distance. On the contrary, the phenomenon does not seem to be similar in case of 2019 (bottom). UAV-NDVI values for the first three flights in 2019 are not following the trend of spectral sensor-based NDVI. It is observed from the given plot (bottom, Figure 17) that the interval between the flights in 2019 is not so regular as in 2018 (top, Figure 17), hence the UAV-NDVI dataset for the year is not optimal to apply curve fitting. The UAV-NDVI values (every 3 day) were extracted for both years from the spline fitted NDVI curves (see Appendix E) and was eventually utilized for checking the accuracy of the fit. The NDVI values from the fitted curve were positively correlated (RMSE: 0.104; $r=0.92$ & RMSE: 0.016; $r=0.94$) with the spectral sensor NDVI measurements for 2018 and 2019, respectively (Table 5).

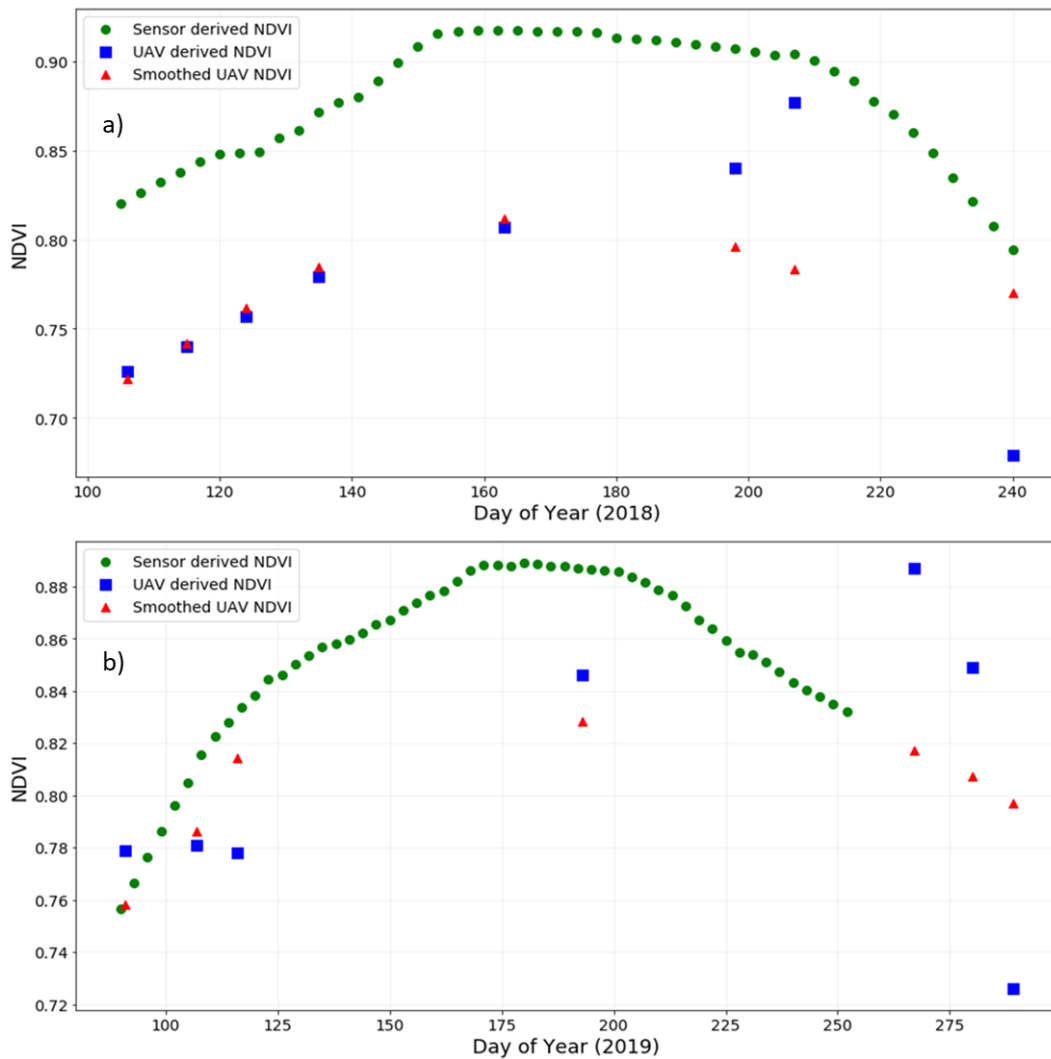


Figure 17. NDVI values extracted from UAV (blue square markers) and spectral sensor (green dot markers) while the red symbols (triangle) represents smoothed UAV-NDVI values of 2018 (a) and 2019 (b) used for curve fitting process.

5.2 Comparison of Phenocamera-based VIs with spectral sensor NDVI

The phenocamera-based VIs computed for ROI that covered full phenocamera FOV (ROI #5) were compared with spectral sensor NDVI. And the results of our comparisons showed that in Asa Research station, the phenocamera-based index values GCC and ExG in 2018 were highly correlated to spectral sensor NDVI (Pearson's correlation of 0.848 and 0.777, respectively), while VIgreen for the same year had the lowest correlation ($r = 0.719$) to the spectral sensor-based NDVI (Table 6). Similar trend of correlation was observed in 2019 with the GCC and ExG indices being highly correlated to spectral sensor NDVI, with correlation coefficients of 0.80 and 0.798, respectively. On the contrary, the correlation of VIgreen in 2019 with spectral sensor-based NDVI is comparatively higher ($r = 0.773$) than in 2018 (Table 6).

Table 6. Correlation between phenocamera vegetation indices over full field of view (FOV) versus spectral sensor derived NDVI values computed within overlapping footprint of sensor with the phenocamera and UAV-derived NDVI, using Pearson's correlation value

Year	Correlation to NDVI (Sensor)			Correlation to NDVI (UAV)		
	GCC	ExG	Vlgreen	GCC	ExG	Vlgreen
2018	0.848*	0.777*	0.719*	0.670*	0.695*	0.631*
2019	0.800*	0.798*	0.773*	0.669	0.706	0.630
	Statistically insignificant ($p > 0.05$)					

* indicates significance level value less than 0.05.

Figure 18 as shown below visually compares the phenocamera indices: GCC (a), ExG (b), and Vlgreen (c) to the spectral sensor NDVI separately across the growing season of both years.

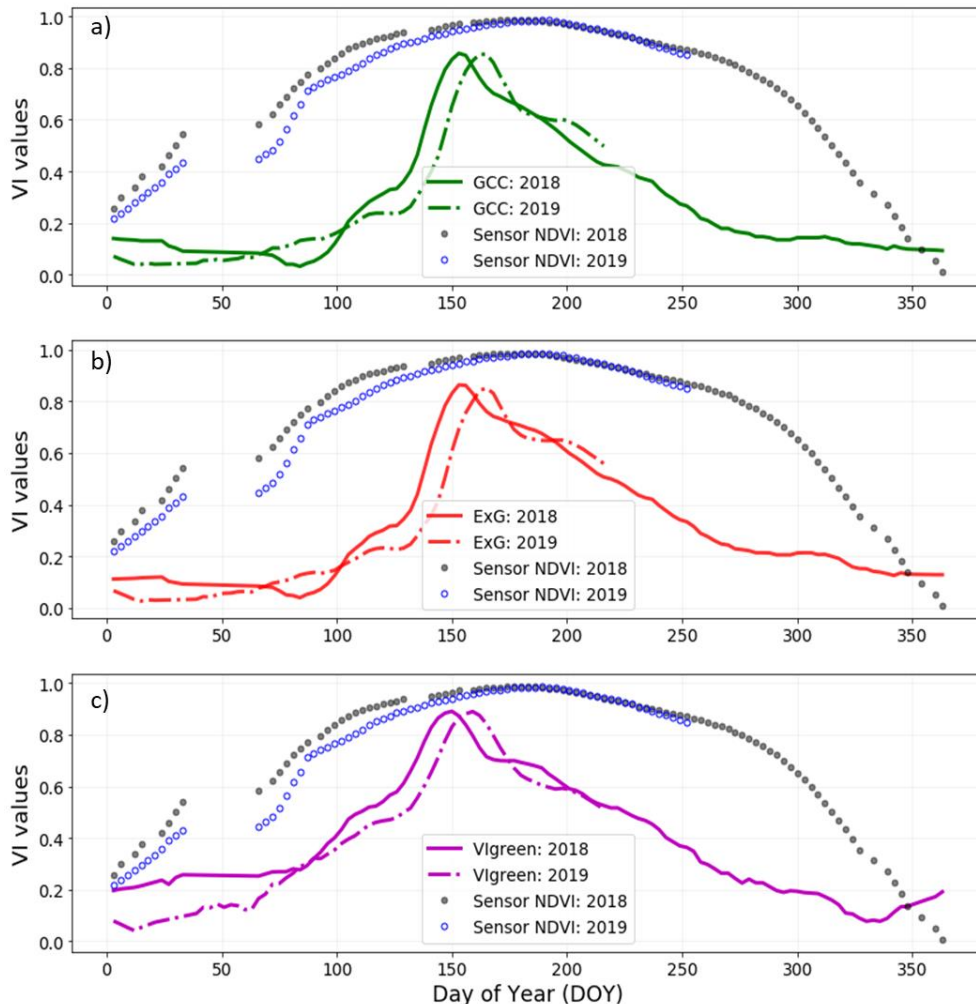


Figure 18. Time series of spectral sensor NDVI (black dots for 2018, blue circles for 2019) and phenocamera-based VIs namely GCC (a), ExG (b) and Vlgreen (c). The y-axis is a normalized scale from indices minimum to maximum values while x-axis is the temporal period of observations. Gap in time series of spectral sensor NDVI refers to removal of low measurements on a snowy day.

It was also noticed considerable disparities between the phenocamera-based indices and spectral sensor NDVI values. The slope of the curve is not so steep in the case of VIgreen. The slopes are steeper in the phenocamera-based indices curves, especially in the case of GCC and ExG, than in the spectral sensor NDVI curve, during both green-up and senescence phase of vegetation growth. This ultimately leads to a narrower season described by the phenocamera and also a bias in phenological transition dates (see Table 8).

5.3 Comparison of Phenocamera-based VIs with UAV-NDVI

The comparison of phenocamera VIs with UAV-derived NDVI (see Figure 19) resulted out positive-good correlation values, but slightly lower than with the spectral sensor-based NDVI values for the year 2018 (Table 6).

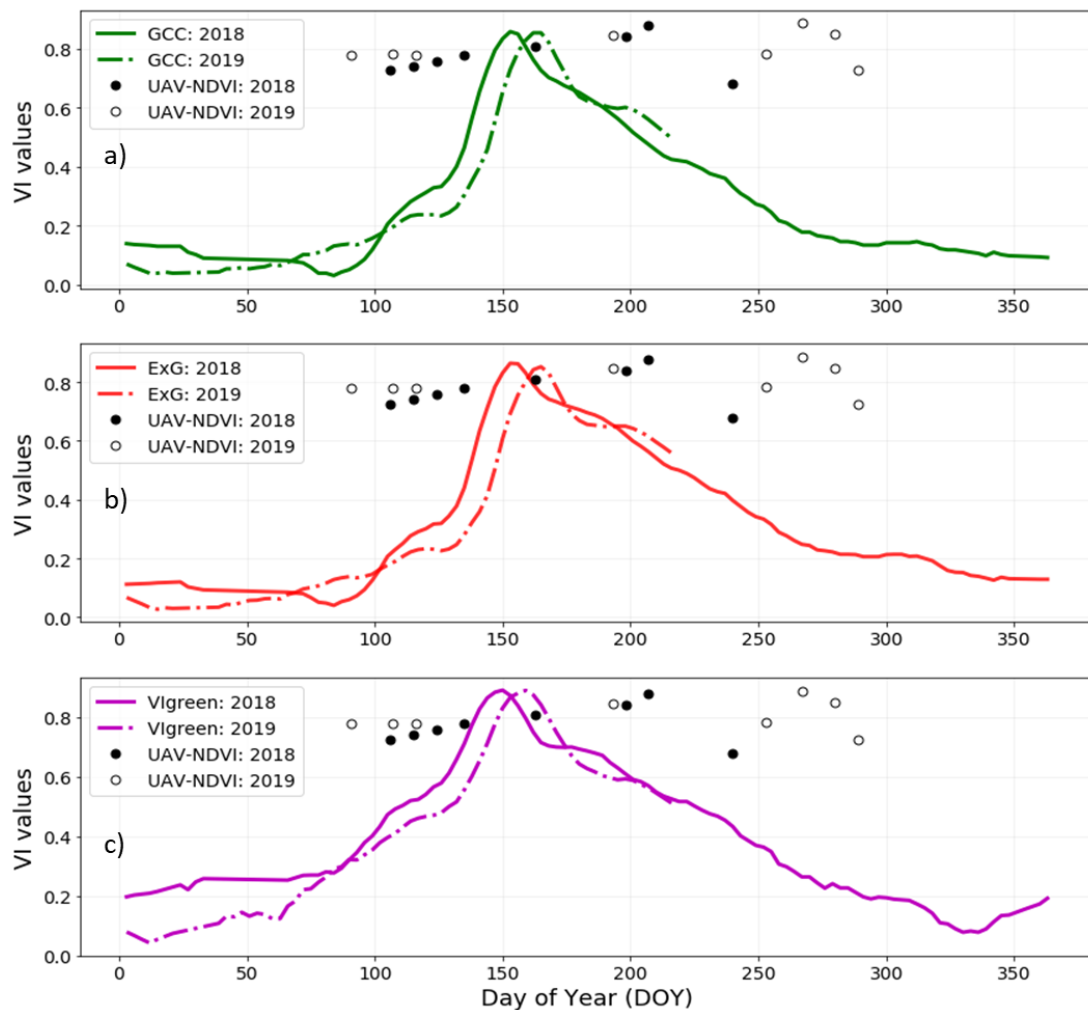


Figure 19. Time series of phenocamera based VIs namely GCC (a), ExG (b) and VIgreen (c) versus UAV-NDVI for both year 2018 and 2019. The y-axis is a normalized scale from indices minimum to maximum values while x-axis is the temporal period of observations. Filled circles (black) and hollow circles (black) represent UAV-NDVI for 2018 and 2019 respectively.

For the same year, GCC and ExG was related well to UAV-NDVI ($r = 0.670$ and $r = 0.695$), while VIgreen was correlated with lowest correlation coefficient ($r = 0.631$). Further experiments on evaluating correlation between UAV-NDVI and phenocamera-based VIs for the year 2019 showed that they are not correlated at all i.e. they are statistically insignificant ($p > 0.05$).

5.4 Annual variability of VIs from Phenocamera

The VI values plot (Figure 18, 19) represents the full phenocamera FOV i.e. ROI #5. A notable seasonal trajectory was observed in the studied area in almost all phenocamera-based vegetation indices:- GCC, ExG and VIgreen. The annual vegetation curves exhibit a sharp rise in GCC and ExG values starting around March, towards an annual peak around May, to slowly drop down to winter dormancy, with a local minima at DOY 330 (Figure 18, Figure 19).

The inter-annual trajectories of phenocamera-based VIs, when compared against each other, allowed to analyse the changes among the information provided by each VI (Figure 19). GCC and ExG for both years are similar and follow the same trajectory, while the peak of the season depicted by VIgreen in both years is not so prominent and present some linear offset, with respect to the other VIs. Upon splitting the VI trajectories into green-up and senescence phase, GCC and ExG are coupled with each other closer in the spring, compared to the fall. The offset distance among VIgreen versus GCC and ExG is seen more clearly in green-up phase, while the three VIs trajectories are closer in the senescence phase. If we compare years 2018 and 2019, all the phenocamera-VIs show a linear shift in the peak of the season, being around 10 days later in 2019. However, the amplitude of the phenological curve remains constant in both years.

Furthermore, an attempt was made to check and quantify how well these phenocamera-VIs correlate among each other.

Table 7. Correlation among phenocamera-based indices: GCC, ExG, and VIgreen

Pearson's Correlation coefficient (r)			
GCC - ExG	ExG-VIgreen	GCC - VIgreen	<i>p</i>
0.981	0.887	0.914	< 0.001
0.994	0.894	0.921	< 0.001

The Pearson’s correlation computed between these indices revealed that GCC is highly correlated to ExG for both years 2018 and 2019, respectively ($r = 0.981$ and 0.994), while the ExG index was correlated to VIgreen with slightly lower value ($r = 0.887$ and 0.894). In addition, GCC was correlated to VIgreen slightly lower than to ExG but higher than to ExG-VIgreen ($r = 0.914$ and $r = 0.921$) respectively. This is in perfect agreement with what the visual assessment (Figure 18 and 19) reflects.

5.4 Variability of VI trajectories within different ROI

Out of multiple region of interests within camera field of view (Figure 7), two ROIs were interesting to inter-compare.

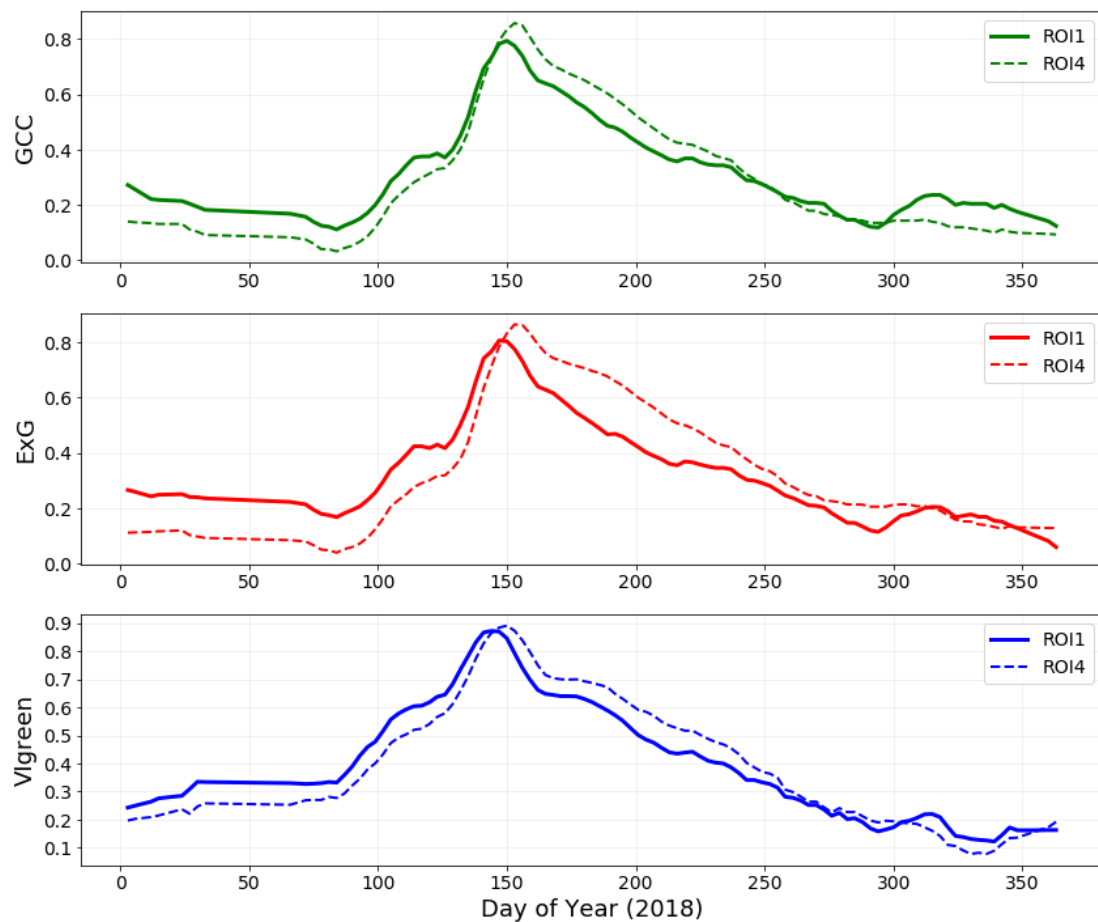


Figure 20. Vegetation indices profiles for 2018 between two different ROIs within phenocamera FOV. Y-axis represents the normalized scale to make VI values appear between 0 and 1.

The two ROIs were ROI #1, characterized as the region focussing individual tree canopy close to phenocamera, and ROI #4 that was the region drawn close to the horizon.

One noticeable thing is the peak of greenness (Figure 20), ROI #4 is reflecting larger amplitude which eventually means the maximum greenness occurs a couple of days to a week later, compared to ROI #1. In addition, the slightly elevated trajectories at the end of the year (after 300th day of year) is smoothened in case of region of interest drawn close to the horizon in the three VIs profiles.

5.5 Phenological dates estimated from different platforms

Phenological transition dates derived from visual inspection demonstrated varying degrees of correspondence to dates identified using different platforms. The phenological dates for different VIs, dates when VIs reach the peak (MAX), and bias of dates when compared to visual estimates are reported for each type of phenocamera-based VIs, UAV and spectral sensor-derived NDVI values (Table 8).

Table 8. Phenocamera-derived VIs (GCC, ExG, VIgreen), spectral sensor-NDVI and UAV-NDVI estimates of Start Of Spring (SOS), Middle Of Spring (MOS), End Of Spring (EOS), Start Of Fall (SOF), Middle Of Fall (MOF), End Of Fall (EOF), visual inspection and maximum of season (MAX) day of year.

Seasonality Parameters	Year	Visual Inspection	Vegetation Indices (DOY)					MAX (DOY)			
			GCC	ExG	VIgreen	NDVI (Sensor)	NDVI (UAV)	GCC	ExG	VIgreen	NDVI (Sensor)
SOS	2018	117	111	111	93	90	112	153	150	147	165
MOS		*	126	129	126	126	136				
EOS		155	147	150	147	162	163				
SOF		*	174	174	174	180	187				
MOF		*	201	207	216	219	235				
EOF		*	240	249	261	261	*				
SOS	2019	120	117	120	90	90	106	159	159	156	183
MOS		*	138	141	126	132	133				
EOS		167	165	165	162	168	163				
SOF		*	180	183	180	186	184				
MOF		*	213	213	210	228	235				
EOF		*	*	*	*	*	265				

*Note: * Refers to lack of the data*
*For the case of visual inspection '**', refers difficulty to define the day of year for corresponding event*

Seasonality parameters mainly the SOS, MOS, EOS, SOF, MOF and, EOF in case of 2018 and 2019 extracted from phenocamera-based VIs were observed to be similar in general when compared among each other, except for the VIgreen, which showed very early SOS and very late EOF. SOS is also early for spectral sensor-based NDVI in both years, compared to GCC and ExG. All VIgreen transition dates were found to be more related (less bias in terms of number of days) to spectral sensor-NDVI. UAV-NDVI

SOS was similar to GCC, and ExG whereas the rest of dates differ having bias of 10 to 34 days in the case of GCC, while 7 to 28 days in the case of ExG). However, the transition dates obtained from UAV-NDVI and spectral sensor NDVI were similar, with a minimum bias (1 – 10 days), except for the SOS. Visually assessed dates (SOS and EOS) compared against dates estimated from the UAV products, phenocamera (i.e., GCC and ExG) and spectral sensor data showed a bias of 5 – 8 days, while the bias is slightly more for SOS estimation from VIgreen and spectral sensor NDVI, with bias ranging between 24 – 27 days in 2018. The estimated day of maximum greenness (MAX) was almost similar in all phenocamera-based indices with spectral sensor NDVI as an exception, where the peak in greenness was achieved slightly later for 2018.

The phenology transition dates between GCC and ExG for year 2019 were well related to each other (maximum difference in transition dates are just 3 days), than 2018 where the difference ranges between 3 – 9 days. The exceptions for year 2019 were also none other than dates estimated from time series of VIgreen and spectral sensor-based NDVI. The transition date for SOS from these two were observed significantly earlier (27 – 30 days) than the rest of the VIs, while UAV data at the same time showed less variation (11 – 16 days). Other parameters achieved from spectral sensor and UAV-NDVI, except the SOS, were quite relatable, meaning that the bias was very small (1 – 7 days). The transition dates from VIgreen and spectral sensor NDVI are very similar in 2018 and 2019. The visual inspection of SOS and EOS date exhibited a very low bias of 2 – 3 days against dates estimated from GCC and ExG in 2019. VIgreen and spectral sensor NDVI resulted SOS 30 days earlier, while EOS was 5 days earlier in case of VIgreen, and 1 day delayed in case of spectral sensor NDVI. The estimated day of maximum greenness (MAX) was almost similar in all phenocamera-based indices, being spectral sensor NDVI an exception, where the peak in greenness occurred very late.

The phenological transition dates of phenocamera indices (GCC, ExG and VIgreen), spectral sensor NDVI, and UAV-NDVI for the year 2019 revealed a seasonality shift of a week to two weeks (Table 8), than the previous year for all the seasonality events.

6 Discussion

In this research, an effort has been made to compare the phenology of a forest defined through different near-surface remote sensing methods. Using combined methods of UAV photography, phenocamera and a spectral sensor, we explored the different phenological trajectories drawn by these platforms and we evaluate the meaning of each to describe a plant community level phenology.

We realized that the year 2019 had slightly different view of forests because of the growth and movement of camera (Appendix F). In addition, the routine of UAV flights in 2019 were different than 2018. So, it was decided to carry out the processing of datasets in 2 separate years. The outcomes of this study showed that UAV photogrammetry is an effective tool as a means to understand the divergent phenological behaviours of plant phenology. A strong positive relationship between UAV-NDVI and spectral sensor NDVI measurements was observed for both study years. However, even though the strong correlation, there is remarkable offset among UAV and spectral sensor, which has implications in terms of quantifying the photosynthetic activity of the forest from each of the two methods except for the year 2019. The reasons behind such behaviour of UAV-NDVI compared against spectral sensor NDVI especially in 2019 can be related to the different precision associated with the sensors, calibration, processing of data, and not enough UAV-NDVI samples. The UAV-NDVI samples in 2019 is accumulated in spring and fall making a big gap in the middle of the summer, which biases the curve. Despite the offset between spectral sensor NDVI and UAV-NDVI in 2018, the UAV curve follows nicely the spectral sensor curve. The relationship between NDVI from UAV and spectral sensor shows that it is important to cover all the season with regular flights, if we want to have a smooth curve leading to find the transition dates accurately. To determine, if the spline interpolation technique was not overfitting the seven UAV-NDVI values, the samples for the same DOY as that of spectral sensor were used to calculate the correlation and RMSE against the spectral sensor NDVI. These parameters also support the correlation between UAV and spectral sensor NDVI. Both approaches show that these sensors follow the same trend, although it is clearly seen that there is a linear offset between the phenology trajectory of both platforms (UAV and spectral sensor) and they did not perform similarly in 2018 and 2019. When the phenological transition dates extracted

from UAV-NDVI and spectral sensor NDVI are compared, it is observed that they vary only on 9 days, on an average, to a maximum of 22 days, in the case of the SOS. Given that UAV-derived products are georeferenced, the UAV-based phenology parameters can be valuable assets for the validation of other phenology-related remote sensor, such as satellite imagery, as ground truth data. The background cover in a forest stand and individual trees, which can affect the phenology transition estimates, can also be studied using UAVs, given the fine spatial resolution. This is an advantage, in comparison to satellite data, which can study ecosystem dynamics, but not at such level of details.

Of all the studied phenocamera-based VIs, GCC were most closely correlated with the time series of both spectral sensor- and UAV-NDVI (except for the year 2019, where there is no correlation at all between phenocamera VIs and UAV-NDVI). GCC and ExG showed high correlation with spectral sensor NDVI at Asa, suggesting that both platforms are capturing the same vegetation green-up. On the contrary, VIgreen was not so strongly correlated to both spectral sensor- and UAV-NDVI, which was completely unexpected as it was designed to mimic NDVI index. This finding is in agreement with a current study (Peter et al., 2018). Nevertheless, Pearson's correlation values for VIgreen against spectral sensor NDVI slightly improved for the year 2019. On the other hand, phenocamera VIs were not correlated at all (statistically insignificant i.e. $\rho > 0.05$) to UAV-NDVI for 2019, which can be explained by number of records for phenocamera and UAV, are very different (hundreds vs. five). In addition, many UAV records could not be compared against similar dates VIs from phenocamera, since they were flown on the fall, when there was no data from phenocamera sensor. And, the rest of UAV records concentrate in spring and are not evenly distributed along the season. In general, we observed that the correlation between phenocamera VIs and UAV-NDVI weaker than between phenocamera VIs and spectral sensor NDVI. One possible reason for this is the different temporal resolution of the phenocamera (hourly) versus the UAV data (nearly a month). Despite the wide use of phenocamera in phenology studies (Peter et al., 2018; Berra et al., 2019; Klosterman et al., 2018), the oblique FOV of these can cause uncertainties in the time series of canopy greenness (Keenan et al., 2014). As the phenocameras are tilted to some extent from the horizontal, they can capture a vertical profile view of the canopy, while UAVs capture the reflectance of the top of canopy. In addition, phenocamera images depict different

objects depending on the sensor-target distance within the image (that were addressed with different ROIs in this study). This also explains the slightly lower correlation values between UAV-NDVI and phenocamera indices, in comparison to spectral sensors VIs, which is in agreement with Peter et al. (2018). As a result of this sensor-target distance variation, it eventually can alter the quality of time series data, as the targets that are far away from the sensor present weaker signals (underestimation) and have higher atmospheric influence than the targets that are close to sensor, which receive strong signals (i.e. overestimation) (Richardson et al., 2009). Based on our results, this phenomena is clearly noticed and the statement holds true only in the case of green-up phase of plant growth. Only if the phenocamera and the UAV were using a similar sensor could answer if this issue has a ecological reason (phenology) or technical reason (sensor precision and processing accuracy).

The shape of the phenocamera-based VIs fitted curve depicted that the VI_{green} was flatter than the other two indices, while GCC and ExG both were almost identical. On the other hand, when compared against the spectral sensor- and UAV-derived NDVI, the phenocamera-based time series fit showed sharp changes in indices values, especially in the green-up phase. At the same time, the time series of NDVI from spectral sensor and UAV seems to be gradually changing throughout the entire growing season, showing a flatter curve than the phenocamera-based indices. This rate of change in indices values in both green-up and senescence affects the time series fitting and phenological transition date estimation, as they were based on the rate of change in curvature of the curve. This is also supported by the results of seasonality dates, for all time series of data:- flatter curves (in our case, phenocamera-VI_{green} and spectral sensor NDVI) have similar seasonality events in general, with the minimum bias in the number of days.

The results of this research suggest that automated digital cameras (UAVs) can be very effective for the identification of seasonality events, as the transition dates derived from UAV nadir imagery match well to visual observation of the beginning and end of the green season (except SOS of 2019). A double logistic function followed by an analysis of the curvature rate change (Zhang et al., 2003) was used in this study to estimate the phenology transition dates, similarly to Li et al., (2019). Except for the UAV data, a similar approach was used to fit the time series and retrieve the transition dates from

phenocameras and spectral sensor. By doing so, we were able to reduce the potential bias associated to different curve fitting and seasonality detection algorithms, which have been observed in White et al., (2014), as no single curve fitting method was proved to be consistently superior for fitting VIs time series (Klosterman et al., 2014). In general, the phenology transition dates (SOS and EOS) from phenocamera were found to be consistently 6 to 8 days earlier than visual inspection and UAV data values in 2018, while the bias is up to 27 days in the case of VIgreen and spectral sensor data for the same year. The maximum bias was seen only for the SOS event. The SOS for 2019 from UAV-NDVI data experienced the maximum bias (14 days) when compared against the visual observation, and in general the bias was larger in 2019, when compared for the same phenology event in 2018. One possible reason for this could be the number of flights during the green-up phase is less than the year 2018 (five flights in 2018, while only three flights for 2019), which eventually might have experienced higher uncertainty in deriving SOS. Furthermore, the estimated phenology dates validation was based on the visual observation data which, itself is not error free (Klosterman et al., 2014).

In 2018, the vegetation green-up (SOS) started 6 – 9 days earlier in comparison to the 2019. The change in temperature and precipitation over the study area could have influenced such delayed occurrence of seasonality events in 2019. Hence, further studies should include climatic variables as a way to answer the shift in seasonality events. Furthermore, the trees were also growing faster and were closer to the phenocamera (the forest is fertilized and the trees are newly planted ones and growth rate is very high up to 1.5m within a period of 2 years (Jakobsen, pers.comm.).

While the georeferencing process of UAV products generate extremely high precision orthophotos, i.e. a decimeter level accuracy (0.02 m in our case), phenocamera images lack the georeferencing information. Hence, in the inter-comparison of phenocamera images and UAV orthophoto, one can anticipate misalignment inaccuracies (Berra et al., 2019). The misalignment of the various spatial data might be one reason on having differing agreement between the studied platforms. In addition, the quality of the data collected by different sensors is not necessarily similar (Zhang et al., 2017) due to various reasons, one significant one being the difference in spectral bands. Because of this, it is to be ensured if the differences are driven by the forest or environmental

factors, or simply just the difference due to inconsistent sensor settings. Apart from this, the other prime source of uncertainty could be the diversity in temporal resolution between the platforms. The frequency of UAV flights conducted per year against the phenocamera (hourly) or spectral sensor (every 10 sec) is extremely different. Such temporal difference could bias the estimated phenological events (Zhang et al., 2017). Out of nineteen flights conducted for the entire study period, only 7 – 8 flights per year remained, after series of quality checks applied for filtering the most reliable data, and they were not captured evenly throughout the time, making sometimes a temporal gap of 77 days (only in case of 2019). This gap was exactly the peak period during the green-up phase, due to which it could entirely miss the phenology event for a season. Therefore, it is suggested to explore if having the nearly identical dates of data acquisition for different methods could improve the correlation among sensors, as well as the phenology transition dates of the vegetation. For the purpose of characterizing the spring events over different species under study using UAVs, it would always be favourable to start data collection a bit earlier than when the season starts and then finish it by the end of the season without having such larger temporal gaps as found in this study. This will allow getting an overview on what the baseline of indices would look like.

Furthermore, this study has opened up new research domain to investigate if the UAV-derived NDVI could be improved with the spectral sensor datasets. The number of images for radiometric calibration, as well as the flight height of the chosen images taken, exhibit variability of DN values over the panels and eventually affect reflectance (Bueren et al. 2015). In addition, other limitations about empirical line calibration method used in this study are that it assumes constant illumination throughout the image, no or uniform atmospheric effects across the image, and a perfect Lambertian reflecting surface (Smith and Milton, 1999). The assumptions do not agree in the case of our UAV flights and also the reflectance panels used in the process would not necessarily tend to be exactly Lambertian. Several other alternatives do exist such as darkest target method. Hence, an attempt to consider other existing methods of radiometric calibration could enhance the result. Lastly, the normalization of UAV images prior to radiometric calibration and the calibration itself (Berra et al., 2017) might also affect the NDVI values. Therefore, an attempt has to be made to quantify the accuracy of NDVI obtained from the normalized images.

7 Conclusions

Automated digital cameras offer the flexibility of defining regions of interest within very fine spatio-temporal resolution images collected by them, and thus allows researchers to model the phenology dynamics in camera's field of view, for either individual or a group of species within a forest stand. In this study, we used digital cameras as the one carried by a UAV and a phenocamera, often termed as near-surface remote sensing, to evaluate forest phenology. Our results confirm that the UAV-NDVI and spectral sensor NDVI measurements are highly correlated ($r = 0.780$ and $r = 0.903$ for 2018 and 2019, respectively).

In the same way, the phenocamera-based indices (GCC, ExG and VIgreen) are also well correlated to spectral sensor-based NDVI ($r = 0.848$, $r = 0.777$, $r = 0.719$ and $r = 0.80$, $r = 0.798$, $r = 0.773$ for 2018 and 2019, respectively). On the other hand, the correlation was slightly lower to UAV-derived NDVI values ($r = 0.670$, $r = 0.695$ and $r = 0.631$, respectively) for the years 2018, while there was no correlation at all between phenocamera-based VIs and UAV-NDVI values for 2019. Our analysis demonstrated GCC as the best approximation to NDVI time series from UAV and spectral sensor, over the study period. In addition, the analysis also revealed a rapid change in greenness in the green-up phase for phenocamera-based indices, compared to any other platform. The time series of GCC over ROIs, one close to phenocamera and the other close to horizon revealed that the sensor-target distance variation in the case of phenocamera indicated problems of over- and under-estimation of signals, affecting the quality of time series data. The spruce forest experienced a shift in seasonality events. Although the shift is clearly seen in transition dates from individual VIs, the transition dates from all the sensors over two studied years showed a shift of 6 – 18 days.

Furthermore, the study also revealed a close relationship between the seasonality parameters (SOS, MOS, EOS, SOF, MOF and EOF) obtained from aforementioned platforms and the visual inspection was used to validate the data. GCC and ExG-based phenology date estimations were consistently more closely associated with the visual assessments of phenology than those obtained from VIgreen and spectral sensor NDVI, for both years. Phenology transition dates derived from time series of GCC and ExG were almost similar in general, while VIgreen as well as spectral sensor data exhibited earlier SOS (24 and 27 days), earlier EOS (8 days) from VI green and delayed EOS (7

days) from spectral sensor NDVI compared against visual inspection data in 2018. VIgreen and spectral sensor data in 2019 displayed earlier SOS (30 days), slightly higher than 2018. EOS in VIgreen was slightly earlier (5 days) in 2019, while in spectral sensor NDVI, the bias was just 1 day. Except SOS (bias ranges 16 – 22 for 2018 and 2019 respectively), the phenology transition dates from UAV-derived NDVI and spectral sensor-based NDVI exhibited minimum bias (1 days in the case of EOS₂₀₁₈ and 5 days in EOS₂₀₁₉).

To summarize, this study showed the potential of large spatial extent coverage and fine spatial and temporal resolutions of UAV photography for capturing species specific robust phenology indices, as opposed to coarser resolution satellite sensors, and could be used to validate various ecosystem models. The combination of phenocamera, spectral sensor and UAV vegetation metrics bring up the possibility of higher spatio-temporal coverage at local scales, and could greatly enhance the understanding of vegetation phenology from overstory and understory perspective.

8 Recommendations

SITES Spectral, a national research infrastructure in Sweden, is doing a great work in collecting a wide range of measurements through the use of both fixed and mobile multispectral sensors, as well as RGB cameras, for monitoring different ecosystems. However, there is always space for improvement regarding data collection, storage as well as data quality and standards associated with it. This research utilized the datasets (UAV, phenocamera, spectral sensor) from Asa station, which allowed to monitor the seasonal dynamics of the spruce forest. For the case of UAV dataset, it is recommended to conduct UAV flights on a regular basis at least once a month. The flight frequency could be adjusted in such a way to cope with the change in vegetation, i.e. making more frequent flights during the main phenological event. This will allow more accurate and reliable comparison of UAV datasets with other sensors. The process of finding GCP markers during the georeferencing of UAV images was very challenging, mainly because of the size of them. Bigger markers would make this work easy and at the same time, more accurate to pinpoint them. The reflectance panels in all flights were placed on top of some black tarp and this made difficulty in extracting DN values for dark panels as they appear almost similar in some of the flights. Radiometric calibration of UAV orthomosaics was based on using several images of reflectance panels captured at the start and end of the mission, but not the orthomosaics itself. This was also related with the size of reflectance panels, as it was impossible to find and extract DN values of them from the orthomosaics itself, because it risks getting DN values of mixed pixels. Therefore, a larger sized reflectance panels should be introduced, which will save a lot of time in radiometric calibration.

Considering the phenocamera dataset, there were a lot of striping effect and extremely bright (lens flare) images, which cut a significant percent of images out of the analysis. The striping effect must be fixed immediately, which will help include all image in analysis. The proper orientation of the phenocamera (facing north), as the documentation suggests, helps minimizing lens flare, shadows, and forward scattering off the canopy. Because of a thunder crash, the electric system that supply power to the phenocamera and spectral sensor failed on August 2019, so no phenocamera images and NDVI measurements for last four months were available, making it impossible to extract EOF and compare it with other sensors data. Therefore, there should be some mechanism to check if the system is capturing the image on a daily basis. If not, it

should be fixed immediately; otherwise it might miss the entire phenological event within that timeframe. In addition, the phenocamera (more possibly due to wind) seemed to have been moved as there is slight change in FOV for the year 2019. The installation and infrastructure monitoring team must make sure that sensor is stable. The dataset of the same year indicated immediate relocation of either the tower to a new location or raising the height of the sensor above the ground, if possible. The relocation of the tower (if it is in plan) is recommended to be made in a way that it facilitates the researcher to have a field of view over a wide spatial extent. This further extends the research domain to look and inter-compare the forest phenology of different species within forest community. The installation of new phenocamera looking into common region of interest can help validate the result of phenocamera itself, see the effect of viewing direction as well as sensor-target distance. The phenocamera with near infrared band can entirely change the way vegetation signals are captured.

References

- Aasen, H., A. Burkart, A. Bolten, and G. Bareth. 2015. Generating 3D hyperspectral information with lightweight UAV snapshot cameras for vegetation monitoring: From camera calibration to quality assurance. *ISPRS Journal of Photogrammetry and Remote Sensing* 108: 245-259. DOI: 10.1016/j.isprsjprs.2015.08.002
- Ahrends, H. E., S. Etzold, W. L. Kutsch, R. Stoeckli, R. Bruegger, F. Jeanneret, H. Wanner, N. Buchmann, et al. 2009. Tree phenology and carbon dioxide fluxes: use of digital photography for process-based interpretation at the ecosystem scale. *Climate Research*, 39: 261. DOI:
- Arko, L., and K. Joshua. 2012. Sensor Correction of a 6-Band Multispectral Imaging Sensor for UAV Remote Sensing. *Remote Sensing*: 1462. DOI: 10.3390/rs4051462
- Berra, E. F., R. Gaulton, and S. Barr. 2019. Assessing spring phenology of a temperate woodland: a multiscale comparison of ground, unmanned aerial vehicle and Landsat satellite observations. *Remote sensing of environment* 223: 229-242. DOI: 10.1016/j.rse.2019.01.010
- Berra, E. F., R. Gaulton, and S. Barr. 2017. Commercial off-the-shelf digital cameras on unmanned aerial vehicles for multitemporal monitoring of vegetation reflectance and NDVI. *IEEE transactions on geoscience and remote sensing* 55: 4878-4886. DOI: 10.1109/TGRS.2017.2655365
- Berra, E. F., R. Gaulton, and S. Barr. 2016. Use of a digital camera onboard a UAV to monitor spring phenology at individual tree level. *2016 IEEE International Geoscience & Remote Sensing Symposium (IGARSS)*: 3496. DOI: 10.1109/IGARSS.2016.7729904
- Bueren, S. K. v., A. Burkart, A. Hueni, U. Rascher, M. P. Tuohy, and I. J. Yule. 2015. Deploying four optical UAV-based sensors over grassland: challenges and limitations. *Biogeosciences* 12: 163-175. DOI: 10.5194/bg-12-163-2015
- Burkart, A., V. L. Hecht, T. Kraska, and U. Rascher. 2017. Phenological analysis of unmanned aerial vehicle-based time series of barley imagery with high temporal resolution. *Precision Agriculture* 19: 134-146. DOI: 10.1007/s11119-017-9504-y
- Chen, J., P. Jönsson, M. Tamura, Z. Gu, B. Matsushita, and L. Eklundh. 2004. A simple method for reconstructing a high-quality NDVI time-series data set based on the Savitzky–Golay filter. *Remote Sensing of Environment* 91: 332-344. DOI: 10.1016/j.rse.2004.03.014
- Chuine, I., Kramer, K., Hänninen, H., 2013. Plant Development Models. In: M.D. Schwartz. (Ed.). *Phenology: An Integrative Environmental Science*. Springer Netherlands, Dordrecht, pp. 275–288. DOI: 10.1007/978-94-007-6925-0_4
- Chuvieco, E. 2016. *Fundamentals of Satellite Remote Sensing. Second Edition*. CRC Press. doi:10.1201/b18954.
- Cui, T., L. Martz, E. G. Lamb, L. Zhao and X. Guo. 2019. Comparison of Grassland Phenology Derived from MODIS Satellite and PhenoCam Near-Surface Remote Sensing in North America. *Canadian Journal of Remote Sensing* 45: 707-722. DOI: 10.1080/07038992.2019.1674643

- Donnelly, A., R. Yu, A. Caffarra, J. Hanes, L. Liang, A. R. Desai, L. Liu, and M. D. Schwartz. 2017. Interspecific and interannual variation in the duration of spring phenophases in a northern mixed forest. *Agricultural and Forest Meteorology*, 243: 55-67. DOI: 10.1016/j.agrformet.2017.05.007
- Eastman, J. R., F. Sangermano, E. A. Machado, J. Rogan, and A. Anyamba. 2013. Global Trends in Seasonality of Normalized Difference Vegetation Index (NDVI), 1982-2011. *Remote Sensing* 5: 4799-4818. DOI: 10.3390/rs5104799
- Elmore, A. J., S. M. Guinn, B. J. Minsley, and A. D. Richardson. 2012. Landscape controls on the timing of spring, autumn, and growing season length in mid-Atlantic forests. *Global Change Biology* 18: 656-674. DOI: 10.1111/j.1365-2486.2011.02521.x
- Gillespie, A. R., A. B. Kahle, and R. E. Walker. 1987. Color enhancement of highly correlated images. II. Channel ratio and “chromaticity” transformation techniques. *Remote Sensing of Environment*, 22: 343-365. DOI: 10.1016/0034-4257(87)90088-5
- Heumann, B. W., J. Seaquist, L. Eklundh, and P. Jönsson. 2007. AVHRR derived phenological change in the Sahel and Soudan, Africa, 1982–2005. *Remote Sensing of Environment* 108: 385-392. DOI: 10.1016/j.rse.2006.11.025
- Hongxiao, J. and L. Eklundh. 2014. A physically based vegetation index for improved monitoring of plant phenology. *Remote Sensing of Environment* 152: 512-525. DOI: 10.1016/j.rse.2014.07.010
- Keenan, T., B. Darby, E. Felts, O. Sonnentag, M. Friedl, K. Hufkens, J. O'Keefe, S. Klosterman, et al., 2014. Tracking forest phenology and seasonal physiology using digital repeat photography: a critical assessment. 24: 1478-1489. DOI: 10.1890/13-0652.1
- Keirith, A. S., L. H. Justin, L. W. Bryce, G. M. Charles, and K. S. Tamzen. 2019. Comparison of Landsat and Land-Based Phenology Camera Normalized Difference Vegetation Index (NDVI) for Dominant Plant Communities in the Great Basin. *Sensors*, 19: 1139-1139. DOI: 10.3390/s19051139
- Klosterman, S., and A. D. Richardson. 2017. Observing spring and fall phenology in a deciduous forest with aerial drone imagery. *Sensors* 17: 2852. DOI:10.3390/s17122852
- Klosterman, S., E. Melaas, J. A. Wang, A. Martinez, S. Frederick, J. O'Keefe, D.A. Orwig, Z. Wang, et al., 2018. Fine-scale perspectives on landscape phenology from unmanned aerial vehicle (UAV) photography. *Agricultural and Forest Meteorology* 248: 397-407. DOI: 10.1016/j.agrformet.2017.10.015
- Klosterman, S. T., K. Hufkens, J. M. Gray, E. Melaas, O. Sonnentag, I. Lavine, L. Mitchell, R. Norman, et al., 2014. Evaluating remote sensing of deciduous forest phenology at multiple spatial scales using PhenoCam imagery. 4305-4320. DOI: 10.5194/bg-11-4305-2014
- Li, X., Y. Zhou, L. Meng, G. R. Asrar, C. Lu, and Q. Wu. 2019. A dataset of 30 m annual vegetation phenology indicators (1985–2015) in urban areas of the conterminous United States. *Earth System Science Data* 11: 881-894. DOI: 10.5194/essd-11-881-2019
- Liu, Y., M. J. Hill, X. Zhang, Z. Wang, A. D. Richardson, K. Hufkens, G. Filippa, D. D. Baldocchi, et al., 2017. Using data from Landsat, MODIS, VIIRS and PhenoCams to

- monitor the phenology of California oak/grass savanna and open grassland across spatial scales. *Agricultural and Forest Meteorology* 237-238: 311-325. DOI: 10.1016/j.agrformet.2017.02.026
- Menzel, A. (2013). Europe. In M.D. Schwartz. (Ed.). *Phenology: An Integrative Environmental Science* (2, pp. 1-5). Springer, New York, London. DOI: 10.1007/978-94-007-6925-0_4
- Michez, A., H. Piégay, J. Lisein, H. Claessens, P. Lejeune. 2016. Classification of riparian forest species and health condition using multi-temporal and hyperspatial imagery from unmanned aerial system. *Environmental Monitoring Assessment*, 188: 146. DOI: 10.1007/s10661-015-4996-2
- My Drone Lab. 2020. 3DR Solo Drone Review: Features, Specifications, Prices, Competitors. [online] Available at: [<https://www.mydronelab.com/reviews/3dr-solo.html>] [Accessed 21 June 2020].
- Park, J. Y., H. C. Muller-Landau, J. W. Lichstein, S. W. Rifai, J. P. Dandois, and S. A. Bohlman. 2019. Quantifying Leaf Phenology of Individual Trees and Species in a Tropical Forest Using Unmanned Aerial Vehicle (UAV) Images. *Remote Sensing* 11: 1534. DOI: 10.3390/rs11131534
- Parrot Store Official. 2020. Parrot SEQUOIA+. [online] Available at: [<https://www.parrot.com/business-solutions-us/parrot-professional/parrot-sequoia>]. [Accessed 21 June 2020].
- Peter, J. S., J. Hogland, M. Hebblewhite, M. A. Hurley, N. Hupp, and K. Proffitt. 2018. Linking phenological indices from digital cameras in Idaho and Montana to MODIS NDVI. *Remote Sensing*, 10. DOI: 10.3390/rs10101612
- Richardson, A. D., S. Klosterman, and M. Toomey. (2013b). Near-surface sensor-derived phenology. In M. D. Schwartz. (Ed.). *Phenology: an integrative environmental science* (2, pp. 413–430). Springer, New York, USA. DOI: 10.1007/978-94-007-6925-0_22
- Richardson, A. D., A. S. Bailey, E. G. Denny, C. W. Martin, and J. O'Keefe. 2006. Phenology of a northern hardwood forest canopy. *Global Change Biology* 12: 1174-1188. DOI: 10.1111/j.1365-2486.2006.01164.x
- Richardson, A. D., B. H. Braswell, D. Y. Hollinger, J. P. Jenkins, and S. V. Ollinger. 2009. Near-surface remote sensing of spatial and temporal variation in canopy phenology. *Ecological Applications* 19: 1417-1428. DOI: 10.1890/08-2022.1
- Richardson, A. D., K. Hufkens, T. Milliman, and S. Frolking. 2018. Intercomparison of phenological transition dates derived from the PhenoCam Dataset V1.0 and MODIS satellite remote sensing. *Scientific reports* 8: 1-12. DOI: 10.1038/s41598-018-23804-6
- Richardson, A. D., K. Hufkens, T. Milliman, and S. Frolking. 2018 (b). Tracking vegetation phenology across diverse North American biomes using PhenoCam imagery. *Scientific Data* 5: 180028. DOI: 10.1038/sdata.2018.28
- Richardson, A. D., J. P. Jenkins, B. H. Braswell, D. Y. Hollinger, S. V. Ollinger, and M. L. Smith. 2007. Use of digital webcam images to track spring green-up in a deciduous broadleaf forest. *Oecologia* 152: 323-334. DOI: 10.1007/s00442-006-0657-z

- Rodriguez-Galiano, V. F., J. Dash and P. M. Atkinson. 2015. Intercomparison of satellite sensor land surface phenology and ground phenology in Europe. *Geophysical Research Letters* 42: 2253-2260. DOI: 10.1002/2015GL063586
- Rossi, S., S. Zhang, A. Deslauries, V. Butto, H. Morin, J.-G. Huang, H. Ren, and S. Khare. 2019. Linking phenocam derived phenology with field observations in the boreal forest. *IEEE* 132-133. DOI: 10.1109/MetroAgriFor.2019.8909272
- Rouse, J.W.; Haas, R.H.; Schell, J.A.; Deering, D.W.; Harlan, J.C. Monitoring vegetation systems in the great plains with ERTS. In Proceedings of the Third ERTS Symposium, NASA SP-351, Washington, DC, USA, 1 January 1974; pp. 309–317.
- Schwartz, M.D. (2013). Introduction. In M.D. Schwartz. (Ed.). *Phenology: An Integrative Environmental Science* (2, pp. 1-5). Springer Dordrecht Heidelberg New York London: Springer. DOI: 10.1007/978-94-007-6925-0
- SLU.SE. 2020. Asa Experimental Forest and Research Station. Available at: [<https://www.slu.se/en/departments/field-based-forest-research/experimental-forests/asa-experimental-forest-and-research-station/>] [Accessed 21 June 2020].
- Smith, G. M., and E. J. Milton. 1999. The use of the empirical line method to calibrate remotely sensed data to reflectance. *International Journal of Remote Sensing* 20: 2653-2662. DOI: 10.1080/014311699211994
- Sonnentag, O., K. Hufkens, C. Teshera-Sterne, A. M. Young, M. Friedl, B. H. Braswell, T. Milliman, J. O’Keefe, et al., 2012. Digital repeat photography for phenological research in forest ecosystems. *Agricultural Forest Meteorology* 152: 159-177. DOI: 10.1016/j.agrformet.2011.09.009
- Toomey, M., A. F. Mark, F. Steve, H. Koen, K. Stephen, S. Oliver, D. B. Dennis, J. B. Carl, et al., 2015. Greenness indices from digital cameras predict the timing and seasonal dynamics of canopy-scale photosynthesis. *Ecological Applications* 25: 99. DOI: 10.1890/14-0005.1
- Tucker, C. J. 1979. Red and photographic infrared linear combinations for monitoring vegetation. *Remote Sensing of Environment* 8: 127-150. DOI: 10.1016/0034-4257(79)90013-0
- Vitasse, Y., S. Delzon, E. Dufrêne, J.-Y. Pontauiller, J.-M. Louvet, A. Kremer, and R. Michalet. 2009. Leaf phenology sensitivity to temperature in European trees: Do within-species populations exhibit similar responses? *Agricultural and Forest Meteorology* 149: 735-744. DOI: 10.1016/j.agrformet.2008.10.019
- White, K., J. Pontius, and P. Schaberg. 2014. Remote sensing of spring phenology in northeastern forests: A comparison of methods, field metrics and sources of uncertainty. *Remote Sensing of Environment* 104 148: 97-107. DOI: <https://doi.org/10.1016/j.rse.2014.03.017>
- White, M. A. and R. R. Nemani 2006. Real-time monitoring and short-term forecasting of land surface phenology. *Remote Sensing of Environment* 104: 43-49. DOI: 10.1016/j.rse.2006.04.014
- Wonpil, Y. 2004. Practical anti-vignetting methods for digital cameras. *IEEE Transactions on Consumer Electronics, Consumer Electronics, IEEE Transactions on, IEEE Trans. Consumer Electron.* 50: 975-983. DOI: 10.1109/TCE.2004.1362487

- Yang, G., Liu, J., Zhao, C., Li, Z., Huang, Y., Yu, H., Yang, H. 2017. Unmanned Aerial Vehicle Remote Sensing for Field-Based Crop Phenotyping: Current Status and Perspectives. *Frontiers in Plant Science*, 8. DOI: 10.3389/fpls.2017.01111
- Zhang, X., M. A. Friedl, and C. B. Schaaf. 2006. Global vegetation phenology from Moderate Resolution Imaging Spectroradiometer (MODIS): Evaluation of global patterns and comparison with in situ measurements. *Journal of Geophysical Research: Biogeosciences*. 111: G04017 DOI:10.1029/2006JG000217
- Zhang, X., M. A. Friedl, C. B. Schaaf, and A. H. Strahler. 2004. Climate controls on vegetation phenological patterns in northern mid- and high latitudes inferred from MODIS data. *Global Change Biology* 10: 1133-1145. DOI: 10.1111/j.1529-8817.2003.00784.x
- Zhang, X., M. A. Friedl, C. B. Schaaf, A. H. Strahler, J. C. F. Hodges, F. Gao, B. C. Reed, and A. Huete. 2003. Monitoring vegetation phenology using MODIS. *Remote Sensing of Environment* 84: 471. DOI: 10.1016/S0034-4257(02)00135-9
- Zhang, X., J. Wang, F. Gao, Y. Liu, C. Schaaf, M. Friedl, Y. Yu, S. Jayavelu, et al. 2017. Exploration of scaling effects on coarse resolution land surface phenology. *Remote Sensing of Environment* 190: 318-330. DOI: 10.1016/j.rse.2017.01.001
- Zhao, J.; Zhang, Y.; Tan, Z.; Song, Q.; Liang, N.; Yu, L.; Zhao, J. Using digital cameras for comparative phenological monitoring in an evergreen broad-leaved forest and a seasonal rain forest. *Ecol. Inform.* 2012, 10, 65–72

Supplementary Data

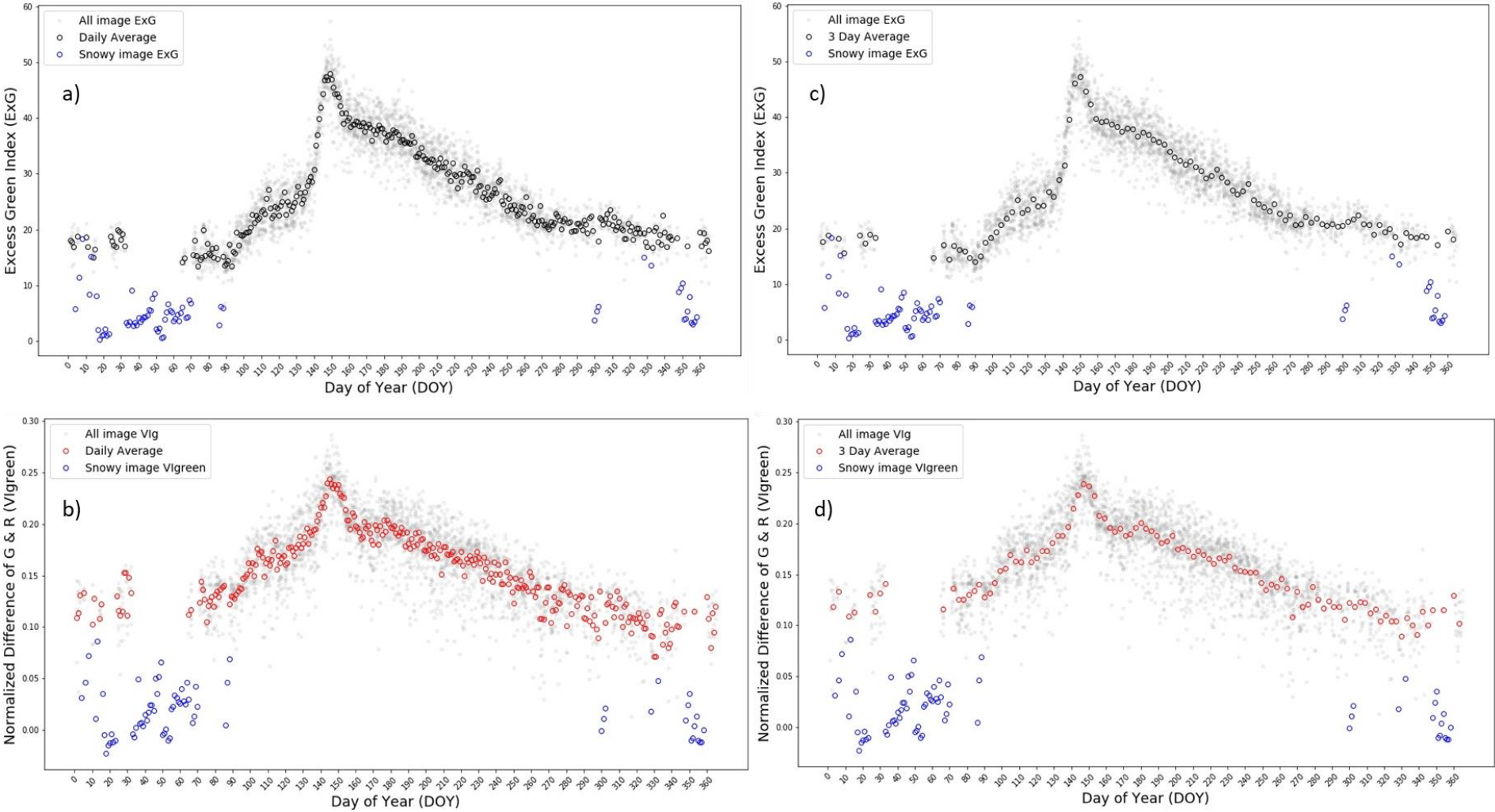
Appendix A:

Table 3. Information on the UAV missions conducted during 2018 and 2019 with corresponding number of images and weather conditions.

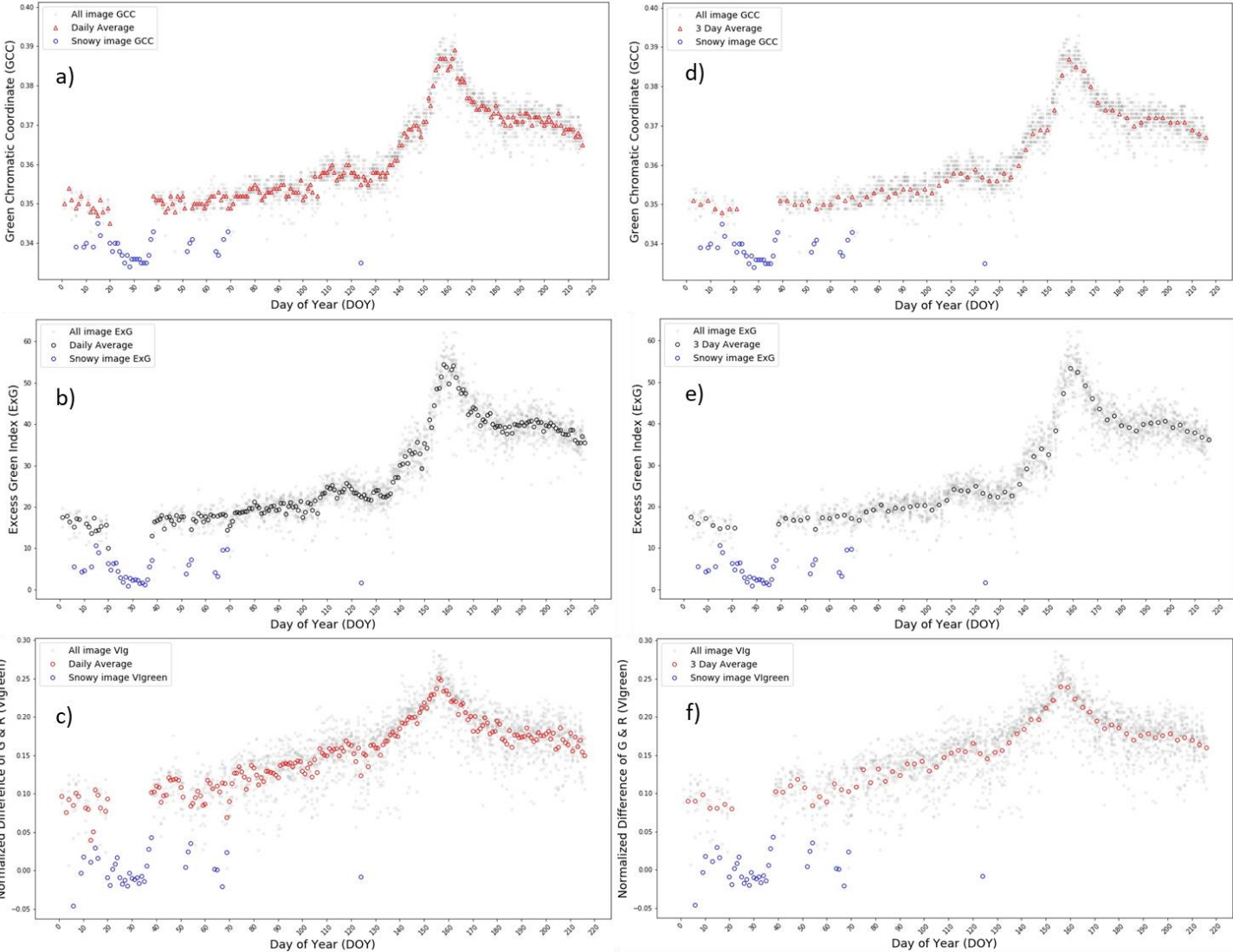
No.	Flight Date	Flying height (m)	Flight time (Local Time)	Number of images	Weather conditions	Status
1	2018-04-16	80	12:20	2233	Cloudy	✓
2	2018-04-25	80	10:30	2170	Cloudy	✓
3	2018-05-04	80	14:15	2088	Partly cloudy	✓
4	2018-05-15	80	13:00	2756	Cloudy	✓
5	2018-06-12	80	12:35	2716	Cloudy	✓
6	2018-06-26	80	09:45	2734	Mixed (Sunny, cloudy)	***
7	2018-07-17	80	12:15	2772	Sunny	✓
8	2018-07-26	80	12:00	2736	Sunny	✓
9	2018-08-28	80	13:45	2780	Cloudy	✓
10	2019-04-01	80	13:00	2694	Sunny	✓
11	2019-04-17	80	09:30	2746	Sunny	✓
12	2019-04-26	80	13:45	2681	Cloudy	✓
13	2019-05-01	80	11:15	2614	Mixed (Sunny, cloudy)	***
14	2019-07-12	80	12:20	2688	Cloudy	✓
15	2019-08-16	80	10:00	2764	Mixed (Sunny, cloudy)	***
16	2019-09-10	80	12:15	2784	Cloudy	✓
17	2019-09-24	80	10:25	2818	Cloudy	✓
18	2019-10-07	80	11:45	2632	Sunny	✓
19	2019-10-16	80	11:30	2708	Cloudy	✓

*** Flights are not processed and hence not used in the research due to large variation in irradiance data during the flight

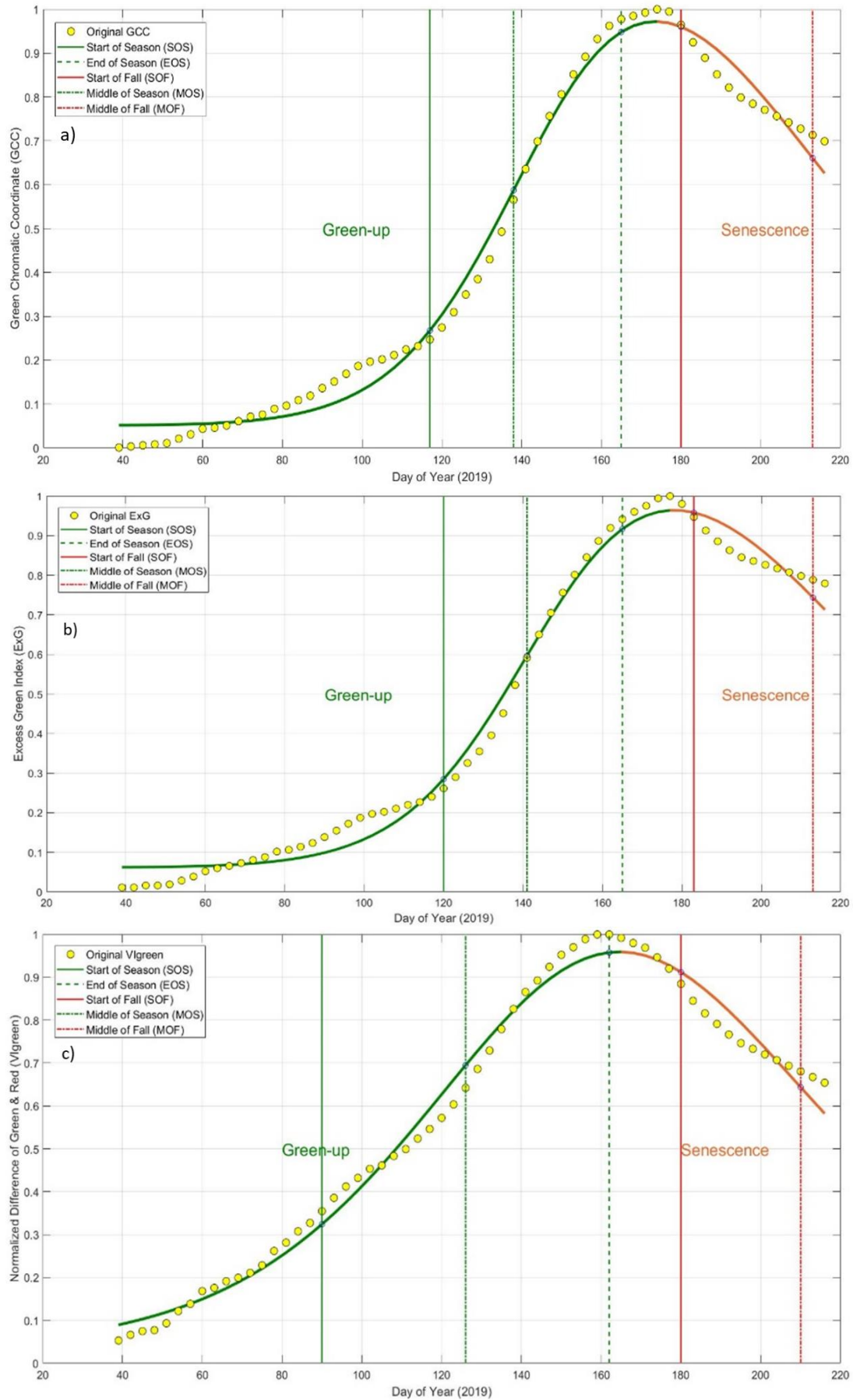
Appendix B: Example of 1-day and 3-day average time series of ExG and Vlgreen for the year 2018. Grey circles are all image average corresponding VI values (every hour) within ROI; blue circles are average respective VI values for snow covered images. Left column represents 1-day average, hollow circles (black) and (red) for ExG (a) and Vlgreen (b) respectively. Right column represents 3-day average ExG (c) and Vlgreen (d).



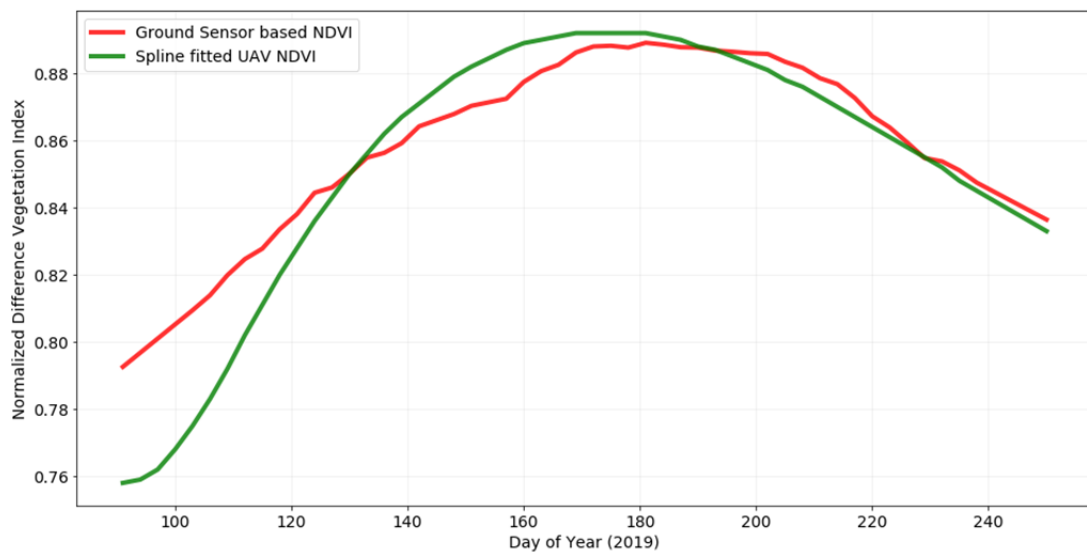
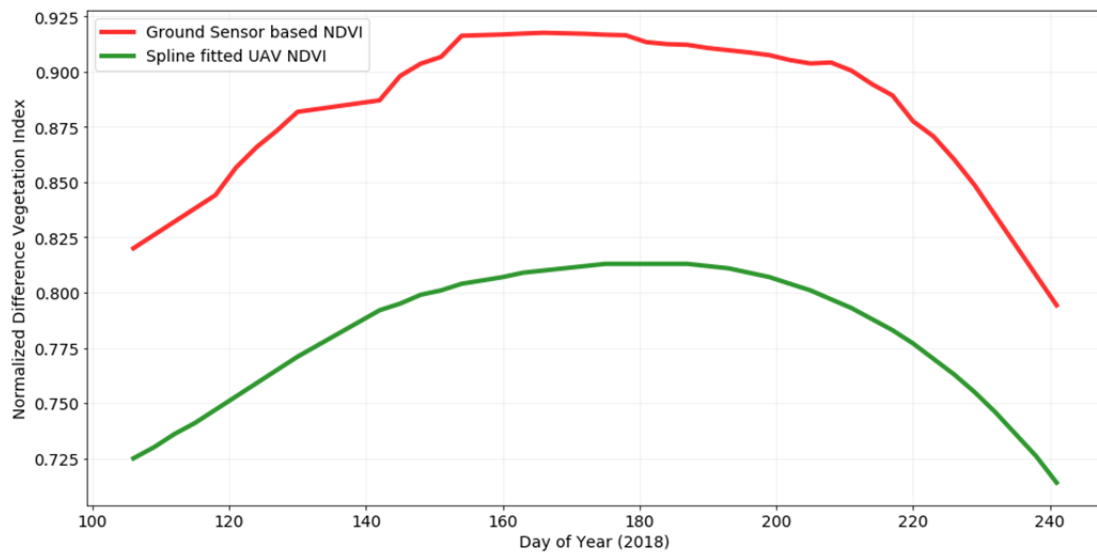
Appendix C: Example of 1-day and 3-day average time series of GCC, ExG and Vgreen for the year 2019. Grey circles are all image average corresponding VI values (every hour) within ROI; blue circles are average respective VI values for snow covered images. Left column represents 1-day average, hollow triangles (red), circles (black) and (red) for GCC (a), ExG (b) and Vgreen (c) respectively. Right column represents 3-day average GCC (d), ExG (e) and Vgreen (f).



Appendix D: Double logistic fit of 3-day averaged time series of GCC (a), ExG (b), and VIgreen (c) and retrieval of phenology transition date from the fit for 2019



Appendix E: Spline interpolation fit to the UAV derived NDVI values after applying smoothing to raw NDVI values of year 2018 and 2019.



Appendix F: Different FOV of the phenocamera sensor possibly caused by the movement due to wind and also due to growth of the vegetation. Upper image is from the year 2018 while lower image is from the year 2019.



2018



2019